Geophysical Journal International

Geophys. J. Int. (2022) **228,** 1294–1312
Advance Access publication 2021 October 1
GJI Seismology

https://doi.org/10.1093/gji/ggab393

Regional lithospheric deformation beneath the East Qinling-Dabie orogenic belt based on ambient noise tomography

Yu Wei,[1] Shuangxi Zhang,[1,2,3] Mengkui Li,[1] Tengfei Wu,[4] Yujin Hua,[5] Yu Zhang[1] and Jianfeng Cai[1]

[1]*Department of Geophysics, School of Geodesy and Geomatics, Wuhan University, Wuhan* 430079, *China. E-mails: shxzhang@sgg.whu.edu.cn; mkli@sgg.whu.edu.cn*
[2]*Key Laboratory of Geospace Environment and Geodesy of Ministry of Education, Wuhan University, Wuhan* 430079, *China*
[3]*Collaborative Innovation Center of Geospace Information Science, Wuhan University, Wuhan* 430079, *China*
[4]*School of Civil Engineering and Architecture, Hubei Polytechnic University, Huangshi* 435000, *China*
[5]*Department of Earth Sciences and Engineering, Taiyuan University of Technology, Taiyuan* 030024, *China*

Accepted 2021 September 14. Received 2021 September 13; in original form 2021 May 14

SUMMARY

The Qinling–Dabie orogenic belt, which contain the arc-shaped Dabbashan orocline and is the world's largest belt of HP/UHP metamorphic rocks, formed by a long-term complex amalgamation process between the North China Block and the Yangtze Block. To understand the collision processes and tectonic evolution, we constructed a 3-D *S*-wave velocity model from the surface to a depth of ∼120 km in the eastern Qinling-Dabie orogenic belt and its adjacent region by inverting 5–70 s phase velocity dispersion data of Rayleigh waves extracted from ambient noise data. Our 3-D model reveals low velocities in the middle–lower crust and high velocities in the upper mantle beneath the orogenic belt, suggesting the delamination of the lower crust. Our results support a two-stage exhumation model for the HP/UHP rocks in the study area. First-stage exhumation was caused by the slab breaking away from the subducted Yangtze Block during the Early–Middle Triassic. Partial melting of the lithospheric mantle caused by slab breakoff-related asthenospheric upwelling weakened the lithospheric mantle beneath the orogenic belt, and continued convergence of the two continental blocks led to further thickening of the lower crust. Such processes promoted lower-crust delamination, which triggered the second-stage exhumation of the HP/UHP rocks. In the Dabbashan orocline, two deep-rooted high-velocity domes, that is, Hannan–Micang and Shennong–Huangling domes, acted as a pair of indenters during the formation stage. High-velocity lower crust was observed beneath the Dabbashan orocline. In addition, our 3-D model reveals that high-velocity lithospheric mantle extends from the Sichuan Basin to the Dabbashan orocline, with a subhorizontal distribution, providing strong support for the high-velocity lower crust. We also observed the destruction of lithospheric mantle beneath the Yangtze Block; the destruction area is bounded by the North–South Gravity Lineament, suggesting that the destruction mechanism of the Yangtze Block may be similar to the North China Block.

Key words: Asia; Seismic noise; Seismic tomography; Crustal structure; Dynamics of lithosphere and mantle.

1 INTRODUCTION

The Qinling-Dabie orogenic belt (QDOB) is a suture zone in Central China that formed by a long-term complex amalgamation process between the North China Block (NCB) and the Yangtze Block (YZB) in Central China. It is one of the most important collision orogenic belts in East Asia and has a complex lithospheric structure (Zhang *et al.* 1995; Meng & Zhang 2000; Ernst *et al.* 2007; Dong *et al.* 2011, 2015; Teng *et al.* 2014; Meng 2017). Multistage tectonic evolution and continuous inland collision resulted in strong and complex compression deformation (Zhang *et al.* 1996b; Hu *et al.* 2012). The QDOB is also the world's largest belt of HP/UHP metamorphic rocks, making it an ideal laboratory for studying the inland collision, deep subduction processes of the orogenic belt, and distribution of metal mineral resources in the mainland of China (Mattauer *et al.* 1985; Enkelmann *et al.* 2006; Ernst *et al.* 2007;

© The Author(s) 2021. Published by Oxford University Press on behalf of The Royal Astronomical Society. All rights reserved. For permissions, please e-mail: journals.permissions@oup.com

Downloaded from https://academic.oup.com/gji/article/228/2/1294/6378898 by guest on 24 April 2024

Wang *et al.* 2013a, b; Teng *et al.* 2014; Jiang *et al.* 2016; Si *et al.* 2016; Song *et al.* 2018).

During the past decades, numerous studies have been conducted from a variety of aspects to establish the fundamental framework for the evolution of the QDOB and the exhumation mechanism of HP/UHP metamorphic rocks. Based on comprehensive analyses of the geophysics, surface geology, and geochemistry, a 'flyover-type' lithospheric structure of the Qinling orogenic belt was proposed to describe its complex deformation (G. Zhang *et al.* 1996a). The 'flyover-type' model suggested a vertical layered structure containing an upper layer with E–W striking structural lineaments, a flat and rheologically distinct middle layer, and a lower layer characterized by N–S striking zones of geophysical anomalies (Song *et al.* 2018). Studies based on the geochemical characteristics (Gao *et al.* 1999), surface wave tomography (Guo & Chen 2017; Song *et al.* 2018) and receiver functions (He *et al.* 2014a; Huang *et al.* 2014) suggested that the QDOB may have experienced lower crust delamination, which is considered to be a critical process during the evolution of the orogenic belt. By using ambient noise tomography in the DBO, Luo *et al.* (2018) suggested a two-stage exhumation process of HP/UHP metamorphic rocks which were first exhumed to the middle-to-lower crust from great depths by buoyancy during the continental collision processes and then exhumed to the surface in an extension environment associated with the doming and magmatism.

In recent years, the Dabashan orocline (DBS), which is located south of the Qinling orogen, and has a tectonic style similar the Himalaya orocline, has received extensive attention due to its gas/oil potential and classic orocline geometry (Shi *et al.* 2012; Song *et al.* 2018). However, the deep structures of the DBS and the relation between the DBS and SCB remain unclear.

Although tremendous studies have previously been conducted in QDOB, there is a lack of research about the entire orogenic belt (Si *et al.* 2016). To the best of our knowledge, most of the regional velocity models of QDOB mainly focused on the crustal structures. The deep structure of the orogenic belt mainly depends on the velocity model published for mainland China, which has a lower resolution at regional scale. Therefore, high-resolution deep structure maps are necessary to further illuminate the evolution of the QDOB.

In this study, we utilized continuous seismic data from 84 permanent and seven portable stations in the eastern QDOB and adjacent areas to construct a regional-scale crust–upper mantle *S*-wave velocity model. Permanent stations were mainly deployed by the China Earthquake Administration. The portable stations are equipped with broadband sensors (Trillium 120/120P) deployed by Wuhan University (WHU). We estimated the Rayleigh wave phase velocity dispersion curves at periods ranging from 5 to 70 s, and then inverted them to obtain a new 3-D velocity model for the crust and upper mantle. The crustal and mantle structures revealed in this study provide insights into the intracontinental deformation of the eastern QDOB.

2 DATA PROCESSING AND PHASE VELOCITY MEASUREMENT

2.1 Seismic data and processing

We collected continuous seismic data recorded at 84 permanent stations (black triangles in Fig. 1) of the China Earthquake Administration from January 2014 to December 2018 and seven portable broadband stations (blue triangles in Fig. 1) of the WHU from January 2016 to December 2018. Data available for this study are shown in the Fig. S1.

In this study, we only used the *Z* components to extract Rayleigh wave dispersion curves. Following the standard noise cross-correlation processing procedure (Shapiro & Campillo 2004; Bensen *et al.* 2007), we first merged the data fragments and generated daily segments at each station. The daily records were then decimated to 1 Hz and the trend, mean value, and instrument response were removed before the data were further filtered from 2 to 100 s. Cross-correlation functions (CFs) of all station pairs were computed using the MSNoise package (Lecocq *et al.* 2014), 1 hr time windows, and a 30 min overlap. To reduce the effects of earthquake signals, we applied a windsorizing of three times the root mean square (RMS) to each time window (Lecocq *et al.* 2014) and spectral whitening in the period range of 2–100 s. Daily CFs were formed by stacking all hourly CFs to improve the stability of the daily CFs and enhance the signal-to-noise ratio (SNR, Wang *et al.* 2017; Clements & Denolle 2018). The CFs sorted by the interstation distance are shown in Fig. 2. Clear Rayleigh wave signals with a velocity of $\sim$3 km s^{-1} were observed.

2.2 Measurement and quality control of dispersion curves

Before extracting the dispersion curve of each station pair, we estimated the average dispersion curve by combining all station pairs (all CFs) based on the method proposed by Prieto *et al.* (2009) as the reference dispersion curve to help to solve the 2π ambiguity of the phase velocity (cycle skipping). Rayleigh wave phase and velocity dispersion data with periods of 5–70 s were extracted based on the spectral method developed by Ekström *et al.* (2009) according to Aki's theory (Aki 1957) using a package modified from GspecDisp (Sadeghisorkhani *et al.* 2018). The spectral method overcomes the limitation that the interstation distances must be longer than three wavelengths, as required by the time-domain method.(Yao *et al.* 2006; Bensen *et al.* 2007; Lin *et al.* 2008). In the spectral method, this limitation is reduced to approximately one wavelength (Ekström *et al.* 2009; Tsai & Moschetti 2010), which allows us to obtain dispersion curves with a broader frequency band.

To identify and reject erroneous measurements and obtain reliable tomographic results, we used the SNRs of CFs and the interstation distance as criteria for the data selection. The interstation distances must be longer than 1.2 times the wavelength. The period-dependent SNR of Rayleigh waves is defined as the ratio of the peak amplitude in the window of the Rayleigh wave signal to the RMS of the trailing noise for each Gaussian narrow bandpass-filtered CF. The time window of the Rayleigh wave signal is calculated by dividing the interstation distance by a phase velocity range of 2.5–4.5 km s^{-1}. The time window of noise was 300 s at the end of the CFs. We retained only CFs with a SNR $>$10. During tomography, we further discarded phase velocity measurements with traveltime residuals larger than 3 s. Based on the above-mentioned quality control measures, 3733 high-quality dispersion curves were obtained in the 5–70 s band, as shown by the grey lines in Fig. 3.

We compared the average measured dispersion curve (black line with error bar in Fig. 3) with the dispersion curve extracted from the velocity structure of mainland China (cyan dotted line in Fig. 3) proposed by Bao *et al.* (2015a) and the Hubei regional curve established by Wu *et al.* (2020) based on teleseismic event data (blue dotted line in Fig. 3). Our results are very similar to those of previous studies, indicating the accuracy of our measurements.

Downloaded from https://academic.oup.com/gji/article/228/2/1294/6378898 by guest on 24 April 2024

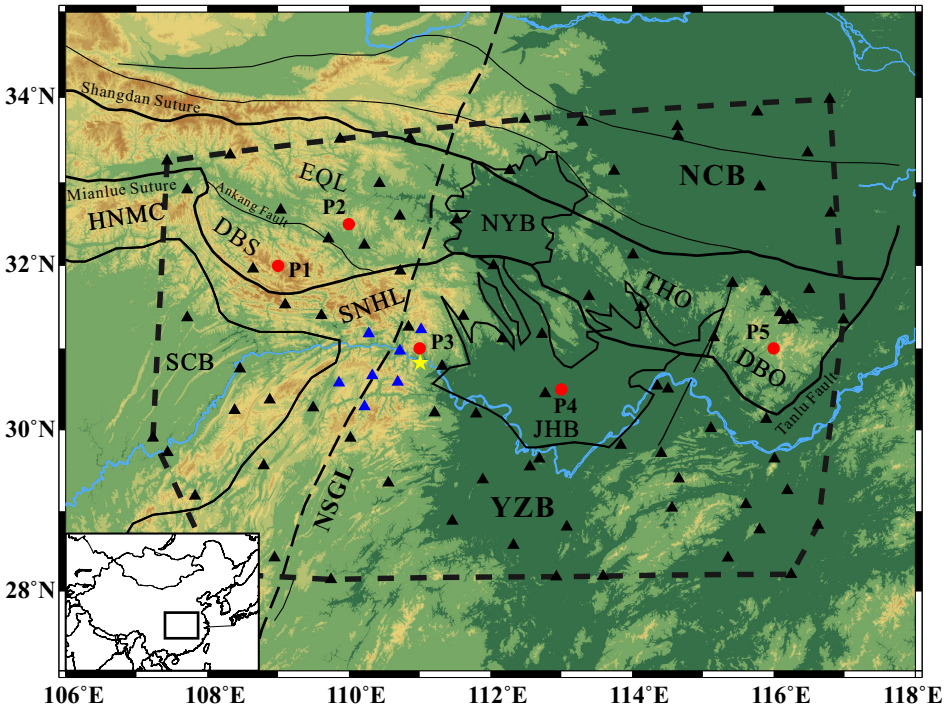

Figure 1. Tectonic map and station distribution in study region. The black rectangle in the lower left inner figure shows the location of the study region in China. The area surrounded by the dark grey dashed line is the main area for tomography. The black triangles represent permanent stations (84), and the blue triangles represent portable stations (7). The yellow stars show location of Three Gorges Dam. The red dots show locations of data fittings in Fig. 10. The black dashed lines denote the North–South Gravity Lineament (NSGL). The thick black lines are the plate and geological unit boundaries. The thin black lines represent faults (modified from Liu *et al.* 2005 and Zhang *et al.* 2009). The main geological units in the study area include Yangtze block (YZB) and North China block (NCB), Jianghan basin (JHB), Nanyang basin (NYB), Sichuan basin (SCB), Eastern Qinling Orogenic belt(EQL), Dabashan orocline(DBS), Tongbai-Hongan Orogenic belt (THO), Dabie orogenic belt (DBO), Shennong-Huangling dome (SNHL) and Hannan-Micang dome (HNMC).

Fig. 3 also shows the phase velocity dispersion curves available at different periods. The number of measured phase velocities reached a maximum of ∼3500 at a period of 20 s and diminished towards both longer and shorter periods due to the fast attenuation of the short-period surface wave energy at short-periods, scattering effect of the complex crustal structure and the limitation of the interstation distance. The ray path coverage of the 8, 20, 40 and 60 s periods is shown in Fig. 4. In most parts of the target area, the ray path coverage is relatively dense and evenly distributed.

3 PHASE VELOCITY TOMOGRAPHY

We divided the study region into a mesh with a grid size of 0.5° × 0.5° and used the surface wave tomography (SWT) package developed by Ditmar & Yanovskaya (1987) and Yanovskaya & Ditmar (1990) to invert the measured phase velocity dispersion data for velocity variation maps at 5–70 s. The SWT is a fast and robust method that has been successfully applied to seismic ambient noise tomography and surface wave tomography (Luo *et al.* 2012, 2013; Guo *et al.* 2013; Zhang *et al.* 2014; Brandmayr *et al.* 2016; Wu *et al.* 2016; Li *et al.* 2017b).

We tested several regularization parameters to identify the optimal value, which balances the smoothness and variance of the solutions. The histograms of data residuals of interstation Rayleigh wave traveltimes are plotted in Fig. 5 for 8, 20, 40 and 60 s with standard deviations of 0.74, 0.76, 1.31 and 1.46 s, respectively. The standard deviations of the traveltime residuals at other periods are similar.

The evaluation of the resolution is critical for ensuring the rationality of the inversion parameters and estimating the minimum discernible features (Wu *et al.* 2020). The resolution of the surface wave tomography primarily depends on the coverage and azimuthal distribution of interstation paths. Yanovskaya (1997) proposed the use of the mean size and the stretching of an averaged area for the estimation of the lateral resolution. The averaged area and stretching represent the correlation length and the azimuth distribution of ray paths, respectively. In this study, we used this method to obtain the resolution maps at 8, 20, 40 and 60 s (Fig. 6). The results show that the resolution at 8–40 s is ∼25–40 km in most parts of the study area, and gradually degrades towards the fringes, where the path coverage becomes sparse. The resolution at 60 s is ∼60–80 km because the ray path number is smaller than that at shorter periods.

We also conducted traditional checkerboard tests to further verify the resolution and robustness of the tomographic inversions (Saygin & Kennett 2010; Borah *et al.* 2014; Wu *et al.* 2020). The input model was constructed with a ±6 per cent phase velocity perturbation of the average phase velocity within each 1° × 1° grid. We calculated the synthetic traveltimes along the path for all station pairs at each period and added random Gaussian noise of 1 per cent to the data. Subsequently, the synthetic velocity model was inverted by using the same inversion parameters as those used for actual data to obtain the retrieved model. Fig. 7 shows the results of the checkerboard tests. Anomalies with a size of 1° × 1° can be recovered well in most parts of the study area. The checkerboard test revealed that the lateral resolution of the study area is ∼50 km, which is half the length of the checkerboard grid size (Lebedev & Nolet 2003). The estimated resolution and results of the checkerboard test indicated

Downloaded from https://academic.oup.com/gji/article/228/2/1294/6378898 by guest on 24 April 2024

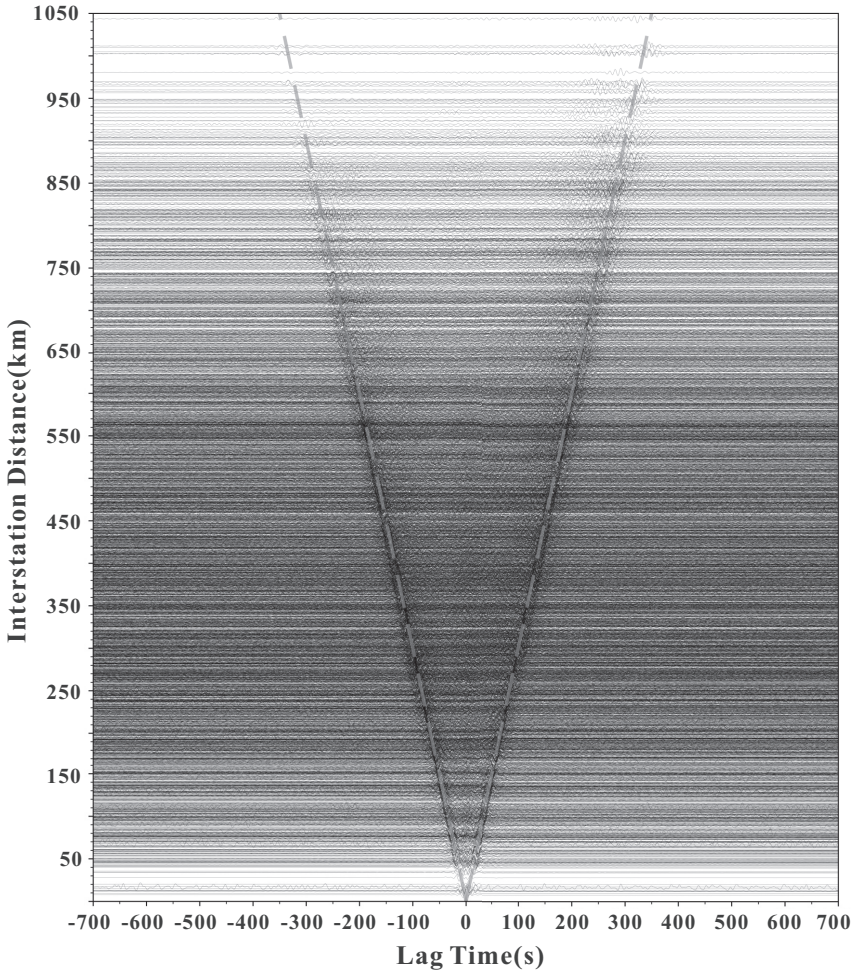

Figure 2. CFs in −700 to 700 s time window filtered between periods of 8–75 s. The grey dash lines display a velocity moveout of 3 km s^{-1}.

that it is reasonable to perform tomographic inversion by dividing the study area into 0.5° × 0.5° grids.

Fig. 8 shows the variation maps of the phase velocities at periods of 8, 20, 40 and 60 s. The phase velocities at the periods of 8 and 20 s (Figs 8a and b) are principally influenced by the structure of the upper-to-middle crust (∼5–30 km), and they are consistent with geological units with low-velocity anomalies in basins and high-velocity anomalies in mountains. Note that the velocity is relativity low beneath DBS, which is consistent with the result of Song *et al.* (2018), Luo *et al.* (2020) and Zhao *et al.* (2021).

At the period of 40 s (Fig. 8c), the imprint of the shallow geological units is gradually reduced, and the phase velocities mainly show the characteristics of depth range of ∼60–80 km. It is notable that the vicinity THO and DBO shows continuous high-velocity anomalies. The result is similar to those of K. Zhao *et al.* (2021) at 40 s. In addition, the DBS and adjacent region show low-velocity anomalies at this period, which is consistent with the result of Luo *et al.* (2020). Prominent low-velocity anomalies are also observed beneath the NCB.

At the period of 60 s (Fig. 8d), corresponding with upper mantle depths (∼80–120 km), the high-velocity anomaly can be observed beneath THO and DBO. The low-velocity anomaly still exists beneath the NCB. In addition, the low-velocity anomaly beneath north of YZB at 40 s still exists at 60 s and the area is gradually increased, which may relate to the lithosphere destruction.

4 3-D *S*-WAVE VELOCITY STRUCTURE

4.1 Model parametrization and *S*-wave velocity inversion

To construct a 3-D V_s model from the phase velocity maps, we adopted an iterative linearized least-squares inversion scheme of surf96 (Herrmann & Ammon 2004; Herrmann 2013) to invert the local dispersion curve at each tomographic grid of a 1-D velocity profile. All the 1-D profiles were combined to create a 3-D *S*-wave velocity model of the crust and upper mantle.

The results of previous studies showed that the inversion result suffers from a trade-off between the Moho depth and *S*-wave velocity (Chen *et al.* 2014; Wu *et al.* 2016). The choice of a proper initial V_s model is vital for obtaining a reliable *S*-wave velocity structure (Luo *et al.* 2012). We construct an initial models (M1) by combining the crustal and mantel structures derived from the 3-D Litho 1.0 model (Pasyanos *et al.* 2014) and the Moho depth (Fig. S2) derived from the receiver function (He *et al.* 2014b).

First, we determined the anchor node for each layer according to the Litho 1.0 and the Moho depth. Smooth models were then obtained based on the spline interpolation of each node. Finally, we divided the interpolated model into several sublayers. To ensure a consistent vertical resolution, the model above 50 km was divided by 2 km and the model below 50 km was divided by 5 km, as shown in Fig. S3.

Downloaded from https://academic.oup.com/gji/article/228/2/1294/6378898 by guest on 24 April 2024

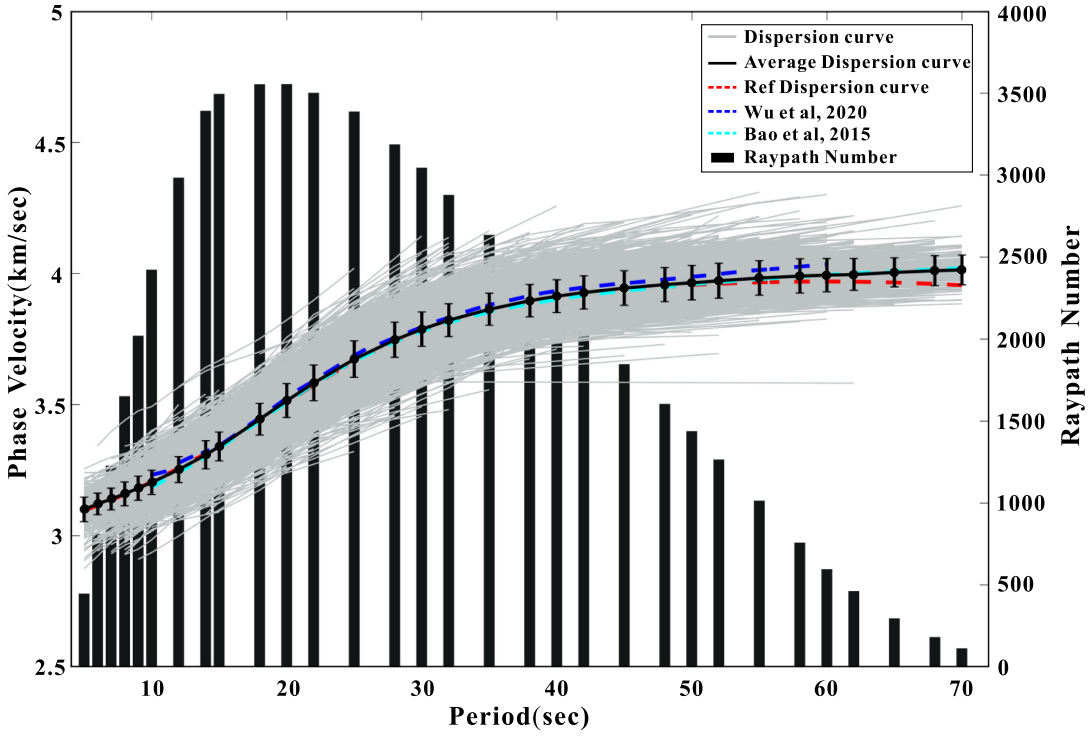

Figure 3. Measured dispersion curves (grey solid line) and the corresponding average values (black solid line) with the associated standard deviation (black bars), respectively. The red dotted line represents the reference dispersion curve used in this study. The blue dotted line represents the result of Wu *et al.* (2020). The cyan dotted line represents the result of Bao *et al.* (2015a). Black histograms represent number of the Rayleigh wave phase velocity dispersion measurements at different periods.

In addition, we also constructed an initial model M2 for comparison. In contrast to the M1 models, the M2 model is a thin-layer model without *a priori* Moho depth and *S*-wave velocity. The velocities of the crust and upper mantle were set to ∼4.5 km s^{-1}. From the surface to a depth of 50 km, the layer thickness was 2 km; it changed to 5 km below 50 km. A similar strategy to construct an initial model was used in the literature (Bao *et al.* 2013; Chen *et al.* 2014; Wu *et al.* 2020).

In both models, the influence of the sedimentary layer was ignored. The fundamental mode of the Rayleigh wave phase velocity is mainly sensitive to the *S*-wave velocity structure at a depth of one-third to half of the wavelength (Li *et al.* 2009). The V_s sensitivity kernels of the Rayleigh wave phase velocity are shown in Fig. 9. The most sensitive depth range is ∼100–140 km at 70 s. Therefore, we were able to obtain a reliable *S*-wave velocity structure of the upper 120 km.

To determine the influence of the initial model and test the inversion parameters, we carried out inversion tests at points P1–P5 in the DBS, EQL, SNHL, JHB and DBO, respectively (red dots in Fig. 1). We inverted the *S*-wave velocity structure at each point by separately using M1 and M2. The inversion was stopped when the standard deviation of the dispersion curve misfits was less than 0.01 km s^{-1}. The maximum iteration number was set to 30. During the first two iterative inversions, the damping value was set to 10 to avoid an overshoot. Subsequently, the damping value was set to 0.1 to balance the trade-off between the model resolution and the damping. A similar inversion strategy was used by Chen *et al.* (2014). The results are presented in Fig. 10. The general patterns of the results inverted from M1 and M2 are similar, which proves that our results are stable and reliable. However, the results inverted from M1 retain the clear Moho constrained by the receiver function result (He *et al.* 2014b) and reveal more details of the crustal and upper mantle velocity structure, which is more consistent with known geological structural units. Therefore, we used the velocity structure obtained by using the initial model M1 for further discussion and research.

The test results also reveal that points in different tectonic units have different *S*-wave velocity structures. At P1 and P4, a lower crustal *S*-wave velocity was observed, which is consistent with the results reported by Luo *et al.* (2020). The high *S*-wave velocity of the upper crustal at P3 may be related to the granite in the SNHL (Luo *et al.* 2020). The high velocity observed in the upper crust at P5 in the DBO agrees with the studies of crustal seismic reflections and the surface geology (Hacker *et al.* 2000) and may be related to the exposure of HP/UHP metamorphic rocks.

At the depth range between the Moho and 120 km, the highest *S*-wave velocity was obtained at P2 in EQL. Similar patterns were obtained for P3 and P4. A decrease below 100 km may indicate LAB beneath these two points. The velocity at P1 increases with the depth and reaches the maximum (∼4.6 km s^{-1}) at ∼110 km, which is consistent with the results reported by Jiang *et al.* (2013).

We inverted the *S*-wave structure of the study region with a grid spacing of 0.5° × 0.5° using the initial model M1 and the same inversion strategy as that used for the initial model test. Because of the limited vertical resolution of surface wave tomography at individual depths (Song *et al.* 2018), we report averaged V_s values for different depth ranges of 5–10, 10–20, 20–30, 30–40, 40–60, 60–80, 80–100 and 100–120 km (Fig. 11). We also provide the results from the inversion using M2 for the same depth ranges as those shown in Fig. 11 for comparison (Fig. S4). Although the inversion results based on the use of the two different initial models have different features in detail at each depth range, the general pattern is similar, which confirms the robustness of our inversion procedure.

Downloaded from https://academic.oup.com/gji/article/228/2/1294/6378898 by guest on 24 April 2024

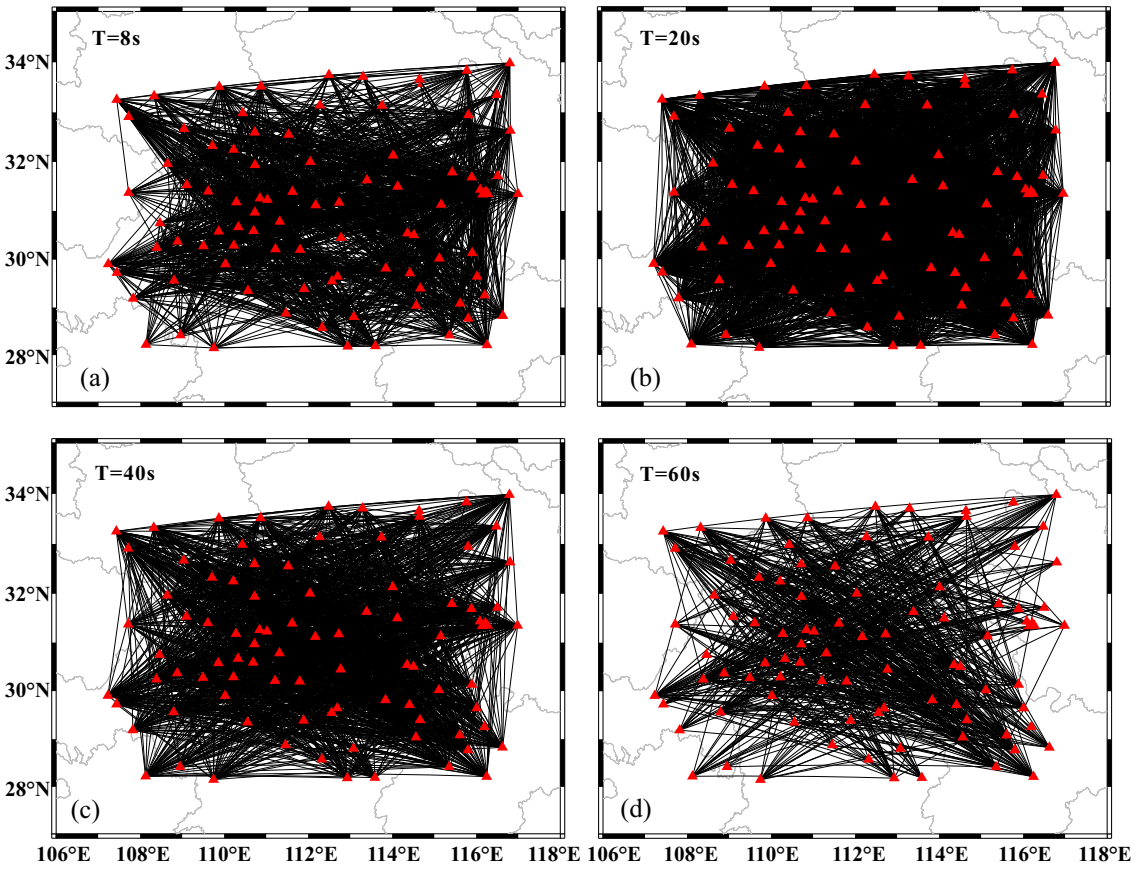

Figure 4. Path coverage of Rayleigh wave phase velocity measurements at 8, 20, 40 and 60s periods. Red triangles show the locations of the stations. Grey line indicates the boundary of provinces, central China.

4.2 3-D MODEL FOR *S*-WAVE VELOCITIES

Based on our newly developed 3-D *S*-wave velocity model, we can discuss the lithospheric structure and the geodynamic evolution of the study area.

At depths of 5–10 km (Fig. 11a), the velocity variations are consistent with the shallow geological units. The low-velocity zones (LVZs) in the basins are closely related to weak sedimentary layers. The high-velocity zones (HVZs) beneath the DBO and THO may be due to the exposure of HP/UHP metamorphic rocks (Wu & Zheng 2013; Guo & Chen 2017; Song *et al.* 2018). The HNMC and SNHL exhibit high-velocity anomalies. There are relatively low-velocity anomalies in the DBS, which are bounded by the high-velocity anomalies of the HNMC and SNHL, which agrees with the results of Song *et al.* (2018) and Luo *et al.* (2020).

At depths of 10–20 km (Fig. 11b), the velocity structures are similar to those in Fig. 11(a), but the contrast is stronger. Prominent LVZs can be observed beneath the JHB, NYB and SCB. Two HVZs exist beneath the HNMC and SNHL domes.

At depths of 20–30 km (Fig. 11c), the velocity structure displays several different details, as shown in Figs 11(a) and (b). The LVZ beneath the JHB fades away, and gradually weaken in NYB. Based on the comparison of Figs 11(a), (b) and (c), the velocity feature beneath the DBO exhibits high anomalies in the upper crust, which decrease in the middle and lower crust. This feature was also reported by Yuan *et al.* (2003), Luo *et al.* (2012) and Zhao *et al.* (2021).

Slice at depths of 30–40 km (Fig. 11d) represent structures in the lower crust or the uppermost mantle. Two consecutive HVZs beneath the HNMC and SNHL domes almost vanish. In this depth range, distinct E–W trending variations in the velocity structures appear and the boundary between high- and low-velocity structures is in good agreement with the surface topography and map of the crustal thickness (Fig. S2), which implies that the eastern areas reach the uppermost mantle, whereas the western areas do not.

At depths of 40–60 km (Fig. 11e), the *S*-wave velocities are greater than ∼4.0 km s^{-1}, indicating that the mantle has been reached in most parts of the study area. Occasionally, relatively low-velocity anomalies can be observed beneath DBS, THO and DBO whereas the velocity anomalies are relatively high in the majority of the study area.

At depths of 60–120 km (Figs 11f–h), several distinct variations in the velocity structures can be observed. First, the general velocity structure differs from that in the shallower depth range. Secondly, a prominent strip-shaped HVZ, marked as HVZ1 in Fig. 11(g), can be observed beneath the EQL, NYB, THO and DBO along the orogenic belt. In addition, HVZ1 gradually vanishes with increasing depth. Third, in the eastern part of the NSGL, notable LVZs, marked as LVZ1 and LVZ2 in Fig. 11(g), appear in the YZB and NCB. They become more notable with increasing depth. The low-velocity structures beneath the SCB, DBS, and EQL in Figs 11(b) and (c) are replaced with high-velocity structures, marked as HVZ2 in Fig. 11(g), leading to a nearly E–W trending velocity structure distribution.

In addition to the average velocity slices with a constant depth range, we also calculated the slices according to the Moho depth (Fig. S2), as presented in Fig. 12. The slices are referred to as the upper crust (upper third of the crust; Fig. 12a), middle crust (middle

Downloaded from https://academic.oup.com/gji/article/228/2/1294/6378898 by guest on 24 April 2024

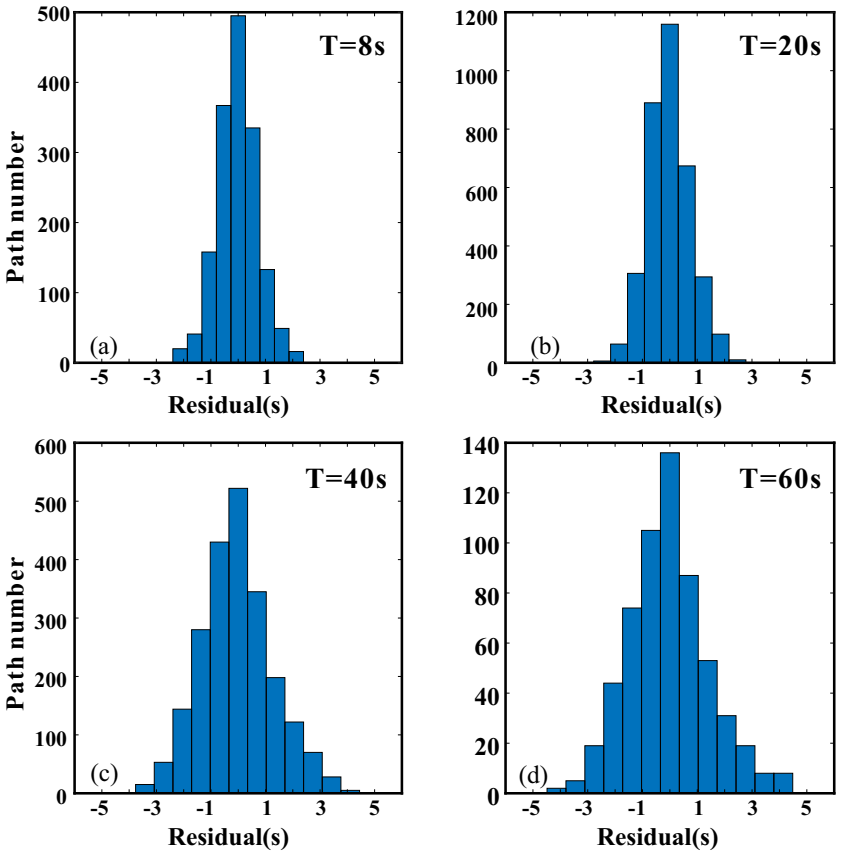

Figure 5. The residual of interstation Rayleigh wave traveltimes at 8, 20, 40 and 60 s.

third of the crust; Fig. 12b), lower crust (lower third of the crust; Fig. 12c), Moho–Moho +20 km depth (Fig. 12d), Moho +20 km–Moho +40 km depth (Fig. 12e) and Moho +40 km–Moho +60 km depth (Fig. 12f). In the upper crust, the velocity structure, which is similar to that shown in Fig. 11(a), correlates well with the surface geology. The SCB, NYB and JHB are dominated by low velocity, whereas the HNMC, SNHL, EQL, THO and DBO are dominated by high velocity. In the middle crust, the LVZ is observed beneath the JHB, NYB and SCB. The HNMC and SNHL are dominated by high velocities. In mountainous areas, the EQL, THO and DBO show relatively low-velocity anomalies that differ from those of the upper crust. In the lower crust, the average velocity patterns significantly differ from those in Figs 11(c) and (d). The significant feature is that the lower crust of the DBS and SCB is dominated by high-velocity anomalies, whereas the lower crust of EQL, THO and DBO displays low-velocity anomalies. The average velocities in the uppermost mantle are shown in Figs 12(d), (e) and (f). In the Moho–Moho +20 km depth range (Fig. 12d), a high-velocity zone (HVZ2) can be observed in the western part of the NSGL beneath the SCB and DBS, whereas a large-scale low-velocity anomaly was detected in the east of the NSGL (LVZ1). A prominent LVZ was observed beneath the DBO, THO and EQL. In the Moho +20 km–Moho +40 km depth range (Fig. 12e), the velocity structure is similar to that shown in Fig. 12(d). The LVZ beneath THO and DBO in Fig. 12(d) is replaced by a relatively high-velocity anomaly. In the Moho +40 km–Moho +60 km depth range (Fig. 12f), HVZ1, HVZ2, LVZ1 and LVZ2 were detected, similar to Fig. 11(g).

To understand our new *S*-wave velocity model, we extracted several vertical velocity profiles, which are presented in Figs 13 and 14. The locations of each profile are shown in Fig. 13(a). A series of significant features was detected in the vertical profiles.

Profiles AA', BB' and CC' are located along the eastern QDOB. Profile AA' is located in QDOB, showing relatively high-velocity anomalies beneath EQL, THO and DOB in the upper crust and low-velocity anomalies beneath the NYB extending to ∼20 km. Another notable feature is the remarkably high-velocity anomaly (HVZ1; V_s ≥4.6 km s^{-1}) in the depth range of ∼60–120 km, which deepens gradually from west to east and presents wavy undulation at the basin-range junction around NYB. This HVZ was also recognized in the models of USTC (Xin *et al.* 2019) and Bao (Bao *et al.* 2015a). Profile BB' includes the HNMC, SNHL, DBS and the frontier of YZB. The two domes show high-velocity anomalies that extend from the near-surface to the lower crust, whereas DBS shows low-velocity anomalies in the upper crust. Significant features in the upper mantle, are the high-velocity zone (HVZ2) in the west and low-velocity zone (LVZ1) in the east. The boundary between the HVZ2 and LVZ1 is highly consistent with the changes in the surface topography and NSGL. We assume that this remarkable feature is related to the destruction of lithospheric mantle in the eastern YZB. Profile CC' includes the HNMC, SNHL, the front of the DBS, and JHB, respectively. The HNMC and SNHL domes show high-velocity anomalies that extend from the near-surface to the lower crust, whereas DBS and JHB exhibit low-velocity anomalies in the upper crust. Note that the lower crust exhibits high-velocity anomalies in the front of DBS. In the upper mantle, we can still observe the HVZ2 west of the NSGL.

Profiles DD', EE', FF' and GG' are in the west of the NSGL. The high-velocity structure beneath the SNHL is clearly delineated in

Downloaded from https://academic.oup.com/gji/article/228/2/1294/6378898 by guest on 24 April 2024

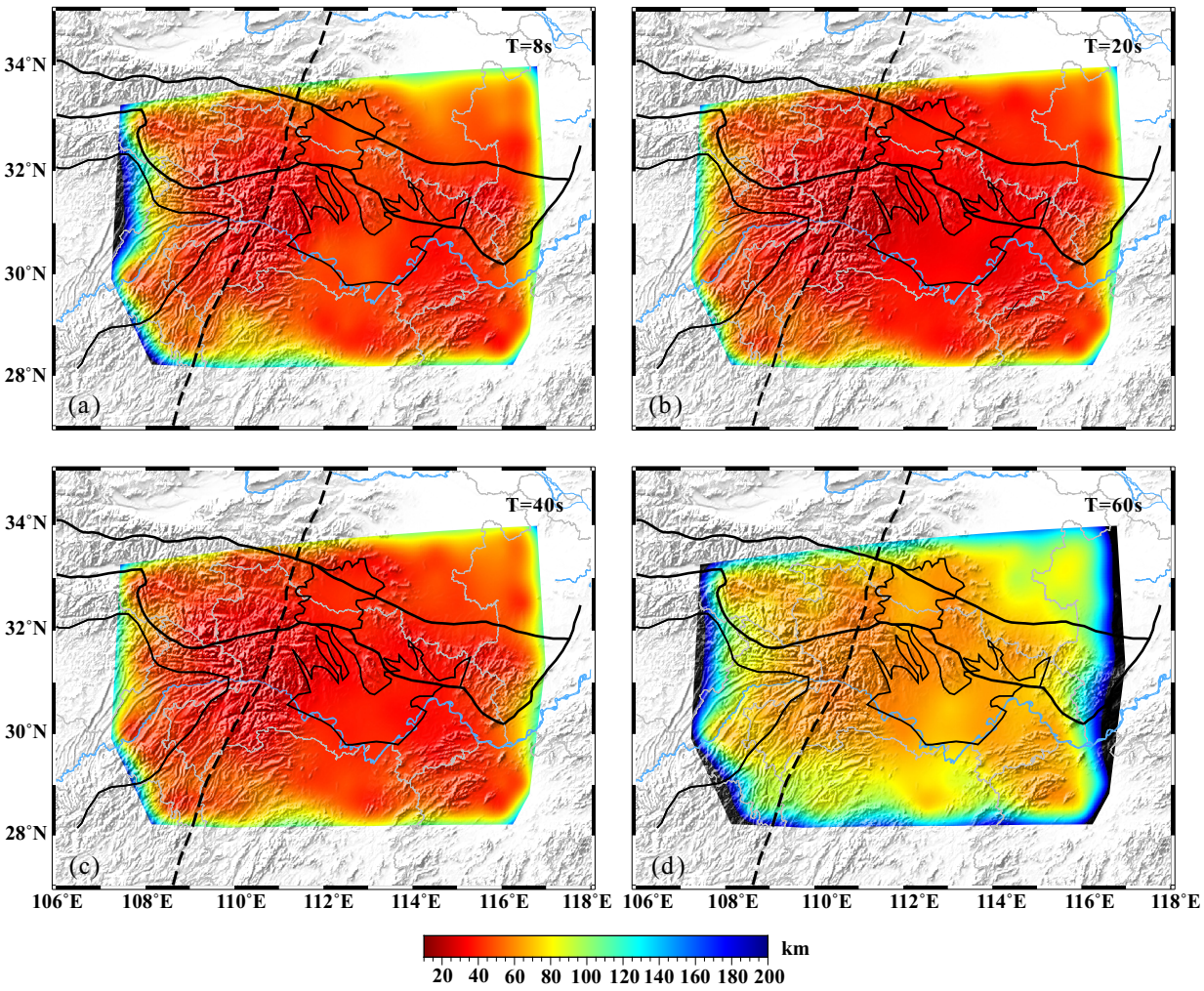

Figure 6. Resolution maps obtained from the mean size of the averaging area in km at 8, 20, 40 and 60 s periods.

profiles FF' and GG'. The continuous high-velocity anomalies of the lower crust beneath the SCB extend to the DBS, which is also shown in Fig. 12(c). The low-velocity anomalies beneath the DBS can be clearly delineated in profile EE'. In addition, a large-scale high-velocity zone (HVZ2; $V_s \geq 4.6$ km s^{-1}) can be observed in the upper mantle. It gradually weakens from west to east (from DD' to GG').

Profiles HH', II', JJ' and KK' are in the east of the NSGL. The JHB is characterized by low-velocity anomalies, while the mountainous regions, such as THO and DBO, are characterized by relatively higher velocity anomalies in the upper crust. The velocity structure of the upper mantle differs from that in the western section, which is more complex. The HVZ1 can be clearly observed beneath THO and DBO. Significant upwelling of the LVZ1 next to the HVZ1 was observed beneath THO and DBO in these profiles, except for profile KK', which is located east of DBO. In addition, we observed high-velocity segments, marked as HVZ3, beneath the YZB, with a slightly lower velocity is than that of HVZ1.

5 DISCUSSION

5.1 Destruction of lithospheric mantle in the YZB

It has been widely accepted that the lithosphere beneath the eastern portion of the NCB has suffered extensive thinning and destruction since the Mesozoic (Gao *et al.* 2009; Xu *et al.* 2013; Yang *et al.* 2018). In the past, numerous studies focused on the lithospheric destruction of the NCB, but relatively few studies have been conducted to analyze the lithospheric destruction of the YZB (Li *et al.* 2015c). However, based on *S*-to-*P* converted waves from over a thousand seismic stations in China, the lithosphere thickness was determined to be ∼80 km below both the eastern NCB and YZB (Shen *et al.* 2019). By reviewing and comparing the tectonic history and lithospheric structure of the YZB and NCB using geophysical, geological and geochemical data, Li *et al.* (2015c) suggested that the eastern part of the YZB has been destroyed.

In our newly proposed *S*-wave velocity model, large-scale low-velocity anomalies (LVZ1 and LVZ2) beneath the YZB and NCB appear below 60 km (Figs 11f–h), which may imply the destruction of the lithospheric mantle. In profiles BB' (Fig. 13c) and CC' (Fig. 13d), a prominent LVZ (LVZ1) can be observed below the Moho. The LVZ1 in the east and HVZ2 in the west are bounded by the NSGL, which means that the destroyed areas are bounded by the NSGL in the west. This feature indicates that the destruction mechanism of the YZB may be similar to the NCB. In profile HH'–KK' (Figs 14e–h) in the east of the NSGL, HVZ3 can be observed in the upper mantle of the YZB, with velocities that are slightly lower than that of HVZ1 beneath the QDOB, and may represent the remnant of the destruction of the lithospheric mantle. The destruction mechanism may be different from that of the orogenic belt. However, additional research is required to confirm the destruction mechanism.

Downloaded from https://academic.oup.com/gji/article/228/2/1294/6378898 by guest on 24 April 2024

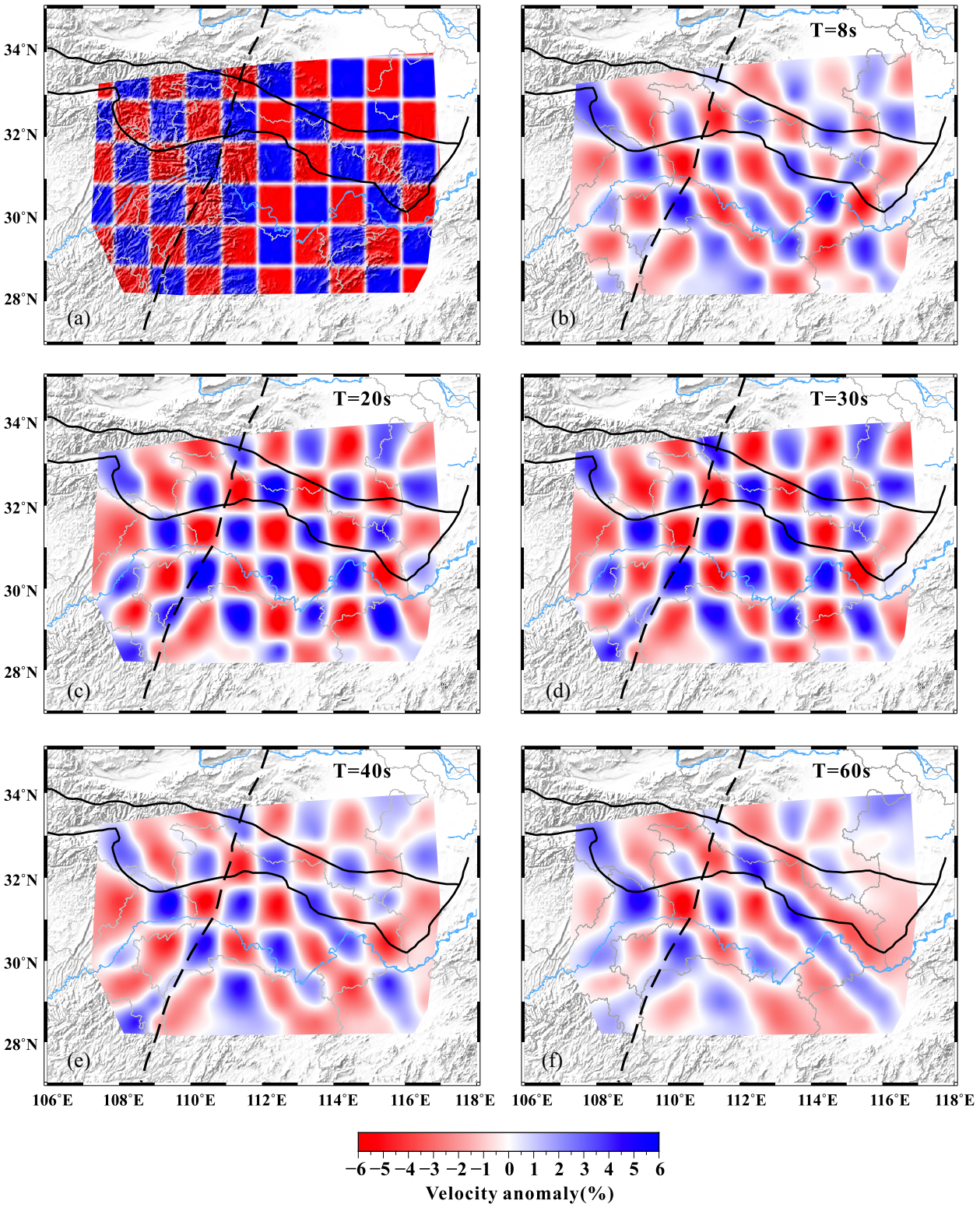

Figure 7. Checkerboard resolution tests and recovery for phase velocities for 10, 20, 30, 40 and 60 s. (a) Input synthetic checkerboard model (anomaly size 1° × 1°) and (b–f) are recovered models at five different periods.

5.2 Lower crust delamination in the east QDOB and exhumation of HP/UHP metamorphic rocks

The QDOB is the world's largest belt of HP/UHP metamorphic rocks, which marks an irregular suture between the NCB and YZB. Its tectonic evolution is diachronous in time and inhomogeneous in space (Li *et al.* 2017a). Due to the wide exposure of UHP/HP metamorphic rocks in the DBO, extensive research has been carried out in this area (Luo *et al.* 2012, 2013, and their references). Results of recent research showed that the UHP/HP metamorphic rocks in

Downloaded from https://academic.oup.com/gji/article/228/2/1294/6378898 by guest on 24 April 2024

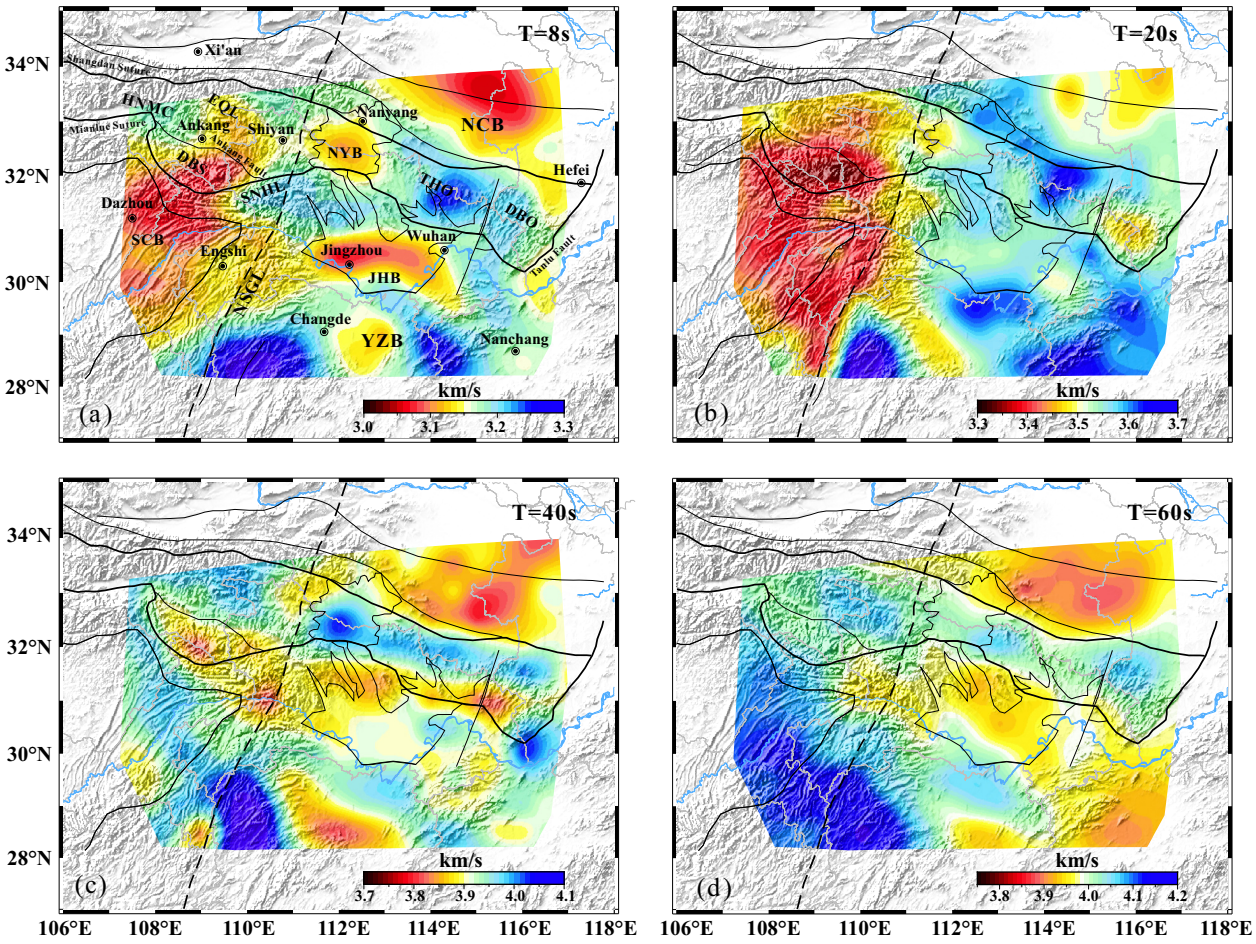

Figure 8. Maps of Rayleigh wave phase velocities at four periods. Panels (a)–(d) are velocity map at 8, 20, 40 and 60 s.

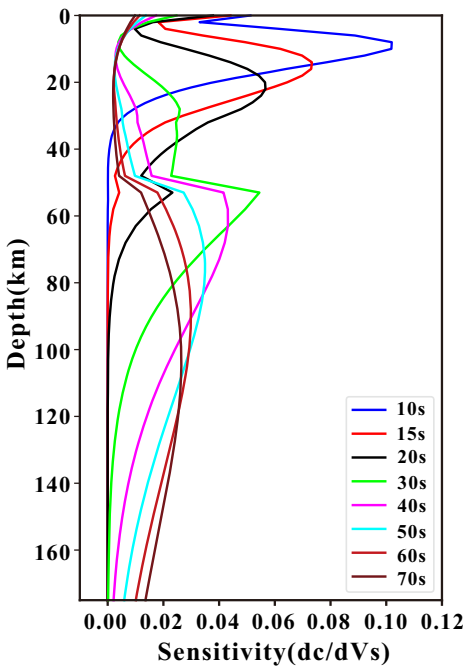

Figure 9. Depth sensitivity kernels of the Rayleigh wave phase velocities at different periods.

THO metamorphic zones have the same ages and characteristics as those in the DBO. These rocks can thus be considered to be coherent (Liu *et al.* 2008, 2015; Wu 2009).

Receiver function and surface wave tomography revealed low-velocity lower crust with lower V_p/V_s ratio beneath the EQL, which indicates that the main composition of the lower crust beneath the Qinling orogen is felsic and the mafic lower crustal layer may have been delaminated in the past (Guo & Chen 2016, 2017). This inference is supported by the models proposed by Song *et al.* (2018) and Luo *et al.* (2020). In our newly proposed *S*-wave velocity model, low-velocity lower crust appears in the EQL, THO and DBO (Fig. 12c). Moreover, the V_p/V_s ratio is lower both in EQL, THO and DBO (Luo *et al.* 2020; He *et al.* 2014a, b). Thus, we suggest that the lower crust delamination may not only occur in EQL, but also in THO and DBO, which is also confirmed by geochemical, petrological and geochronological analyses (Gao *et al.* 1999; Zhang *et al.* 2013; Niu & Jiang 2020). The high velocity in the upper crust reflects the intrusion of HP/UHP metamorphic and/or igneous rocks (Hu *et al.* 2020) and the low velocity in the middle to lower crust reflects the detachment of the mafic lower crustal layer. In addition, the flat Moho and the thin crust beneath EQL, THO and DBO (thinner than global continental crust, Fig. 13b) indicate that there is no mountain 'root' or minor mountain 'root' partially retains beneath the eastern QDOB (Kern *et al.* 1999; He *et al.* 2014a,b), which also supports the lower crust delamination in this region.

Downloaded from https://academic.oup.com/gji/article/228/2/1294/6378898 by guest on 24 April 2024

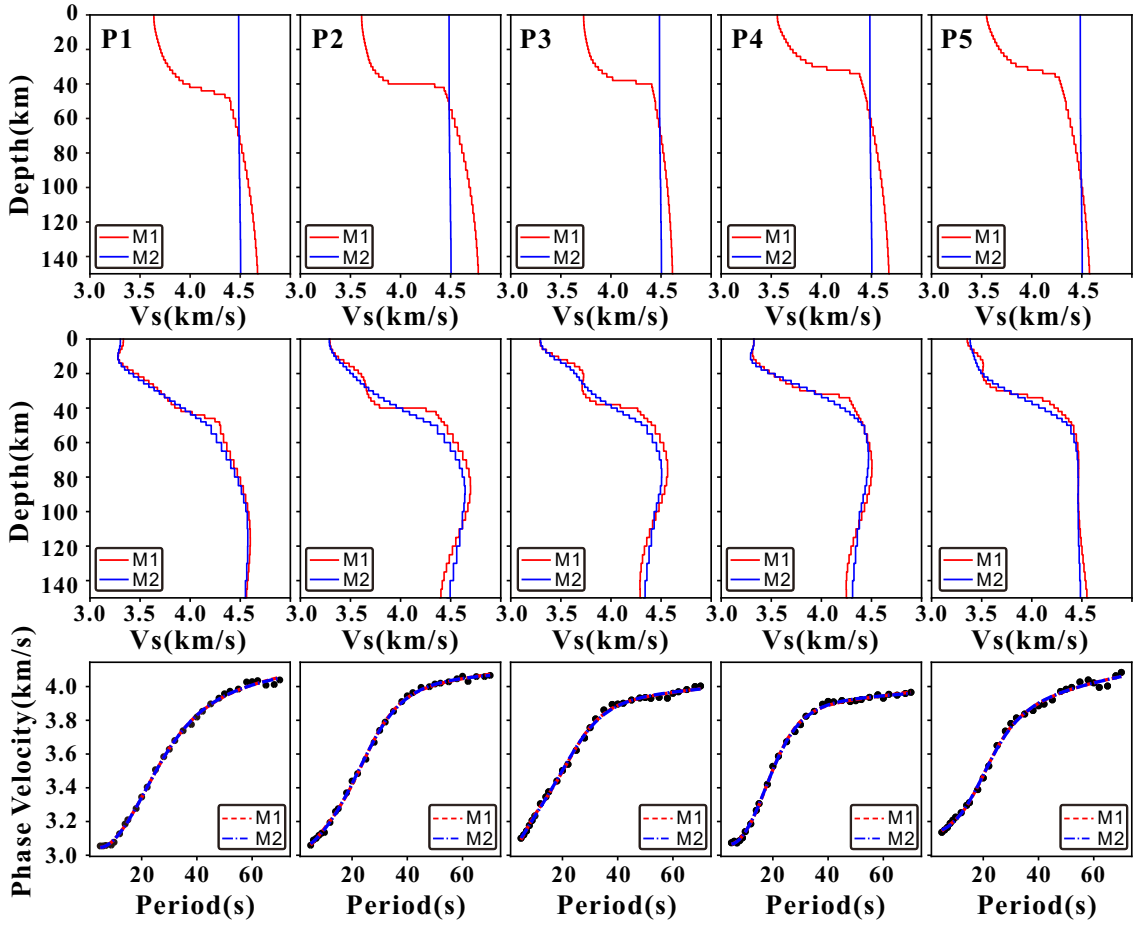

Figure 10. Inverted models and data fit at point P1, P2, P3, P4 and P5. The first row represents the initial model. M1 is constructed by combined the crustal and mantel structure derived from the Litho 1.0 model (Pasyanos *et al.* 2014) and the Moho depth (He *et al.* 2014b). M2 is the initial model without a priori Moho depth and *S*-wave velocity. The second row represents the inversion result. The third row represent the measured dispersion curves (black dots), and the theoretical dispersion curves (red and blue dotted lines) calculated from the final models.

In the uppermost mantle, our model reveals low velocities beneath EQL, THO and DBO. The low-velocity layer gradually thickens from west to east (Figs 12d and 13b). Beneath the low-velocity layer, we can observe a clear HVZ (HVZ1; $V_s \geq \sim 4.6$ km s^{-1}), which can also be observed in Figs 12(e) and (f) and 14(e)–(h). Based on the results of Gao *et al.* (1999), the delaminated thickness of the eclogitized lower crust beneath the QDOB is ∼37–82 km, which is consistent with the spatial scale of the HVZ1 in our model. Laboratory experiments indicate that the seismic velocities of eclogite in the 800–1000 MPa range are greater than those of the neighboring mantle rocks (Kern *et al.* 1999; Wang *et al.* 2005; Zhao *et al.* 2011; Zertani *et al.* 2019). In the profile HH'–KK'(Figs 14e–h), the velocity of HVZ1 is higher than that of HVZ3 in the YZB. Therefore, we infer that the HVZ1 may reflect the eclogitized lower crust delaminated into the upper mantle in the past.

In addition, the upwelling of the LVZ1 presented in profile AA', HH', II' and JJ' due to the lower crust delamination (Gao *et al.* 1999) may be the reason for the intensive magmatism and the wide exposure of UHP/HP metamorphic rocks (Zhao *et al.* 2021).

Geochronological studies and the cooling history of the HP/UHP rocks suggest that the exhumation of HP/UHP rocks to the surface may undergo two stages (Li *et al.* 2005). Based on ambient noise tomography, Luo *et al.* (2012, 2013, 2018) also proposed a two-stage exhumation process for HP/UHP rocks in the DBO. Our new velocity model also supports the two-stage exhumation model. During the Early–Middle Triassic, the YZB and NCB changed from arc–continent collision to continent–continent collision (Wu & Zheng 2013) and the YZB continental lithosphere was dragged down to a depth of more than 100 km by the subducting palaeo-oceanic plate (Wang *et al.* 2005). Based on continuous subduction, the paleo-oceanic slab broke away from the subducted Yangtze lithosphere (Zhao *et al.* 2021). The HP/UHP rocks were exhumed to the depth of the middle or lower crust (Ma *et al.* 1998), which refers to the first stage of the exhumation process of UHP/HP rocks. We found a slab-shape HVZ beneath the eastern QDOB at a depth of ∼400 km by using teleseismic *P*-wave tomography (Jiang *et al.* 2015; He & Zheng 2018), which may indicate that the detached subducted slab sunk to this depth range. Partial melting of the lithospheric mantle caused by slab breakoff-related asthenospheric upwelling weakened the lithospheric mantle beneath the orogenic belt (Li *et al.* 2015b; Bao *et al.* 2015b; Oh & Lee 2019) and continued convergence of the two continental blocks (Li *et al.* 2005) led to further thickening of the lower crust. Such a process laid the foundation for the subsequent lower crust delamination of the orogenic belt, which may have triggered the second stage of the exhumation process of HP/UHP rocks. Fig. 15 shows a schematic model of the present

Downloaded from https://academic.oup.com/gji/article/228/2/1294/6378898 by guest on 24 April 2024

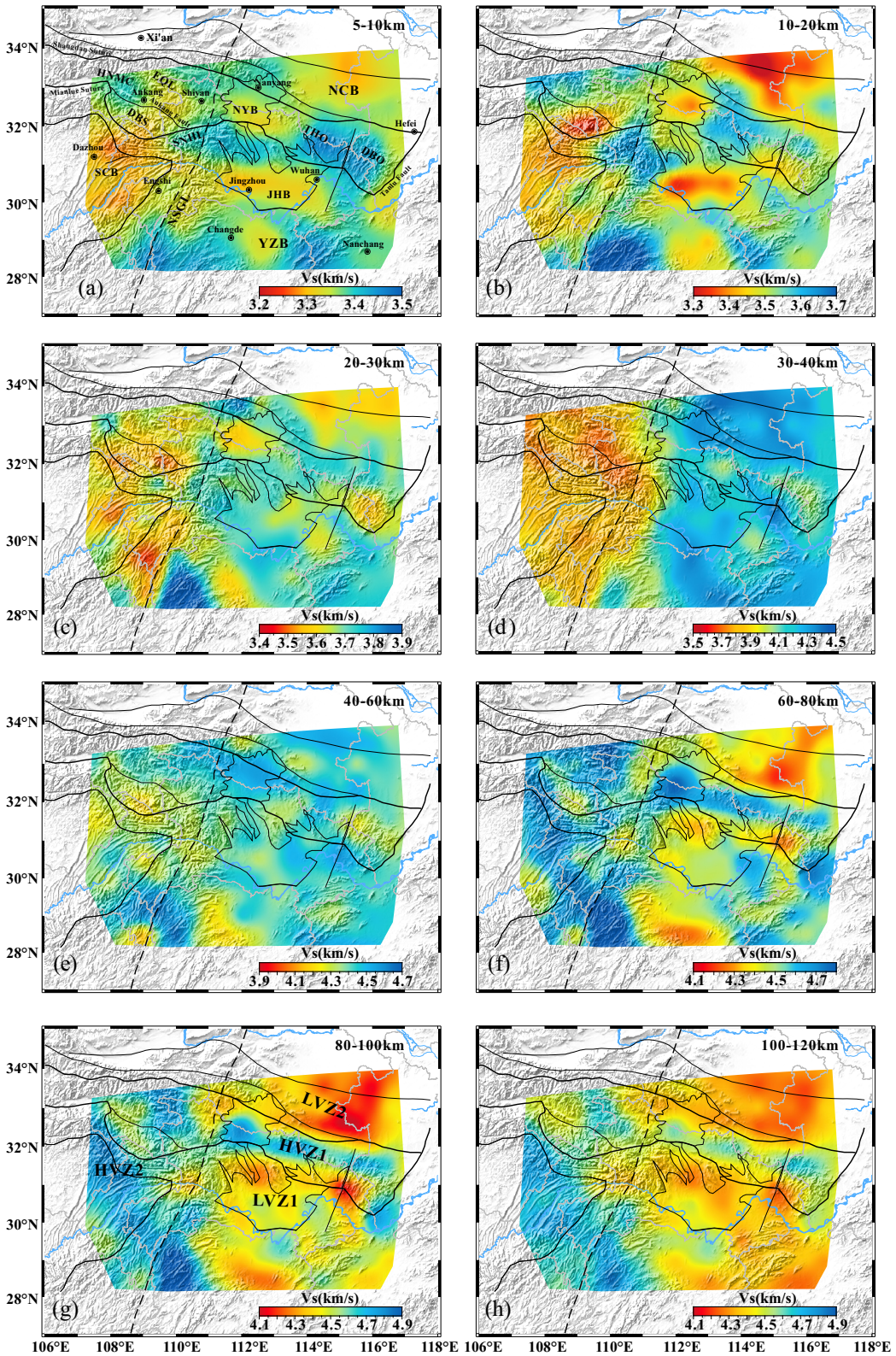

Figure 11. Averaged V_s maps at different depth range. (a) 0–10 km, (b) 10–20 km, (c) 20–30 km, (d) 30–40 km, (e) 40–60 km, (f) 60–80 km, (g) 80–100 km and (h) 100–120 km. HVZ1: upper mantle high velocity zone beneath the QDOB; HVZ2: upper mantle high velocity zone extend from the SCB to DBS; LVZ1: upper mantle low velocity zone beneath the YZB; LVZ2: upper mantle low velocity zone beneath the NCB.

Downloaded from https://academic.oup.com/gji/article/228/2/1294/6378898 by guest on 24 April 2024

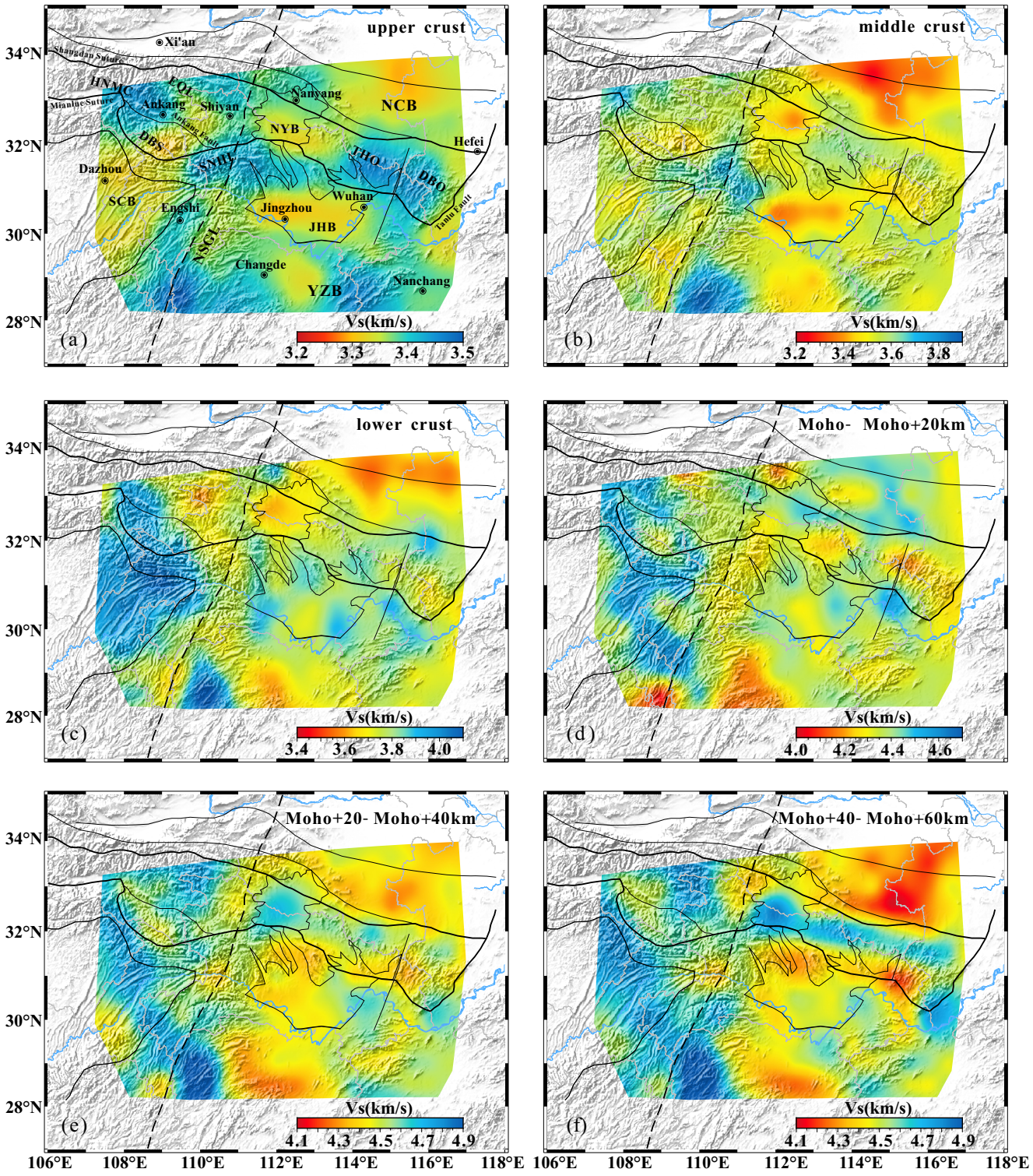

Figure 12. Average *S*-wave velocity slices according to the Moho depth. The upper crust refers to upper third of Moho depth, the middle crust refers to the middle third of Moho depth, the lower crust refers to lower third of Moho depth.

tectonic scene beneath DBO, which is based on the integration of our new tomographic results.

The numerical simulation results show that the rate of delamination is closely related to the effective viscosity of the lithospheric mantle (Wang *et al.* 2011; Chen & Huang 2017). The rheological model of the QDOB revealed that the lithospheric mantle beneath the central and eastern QDOB is relatively strong (Deng *et al.* 2017), which may be responsible for the delaminated eclogitized lower crust to remain in the current depth range.

Downloaded from https://academic.oup.com/gji/article/228/2/1294/6378898 by guest on 24 April 2024

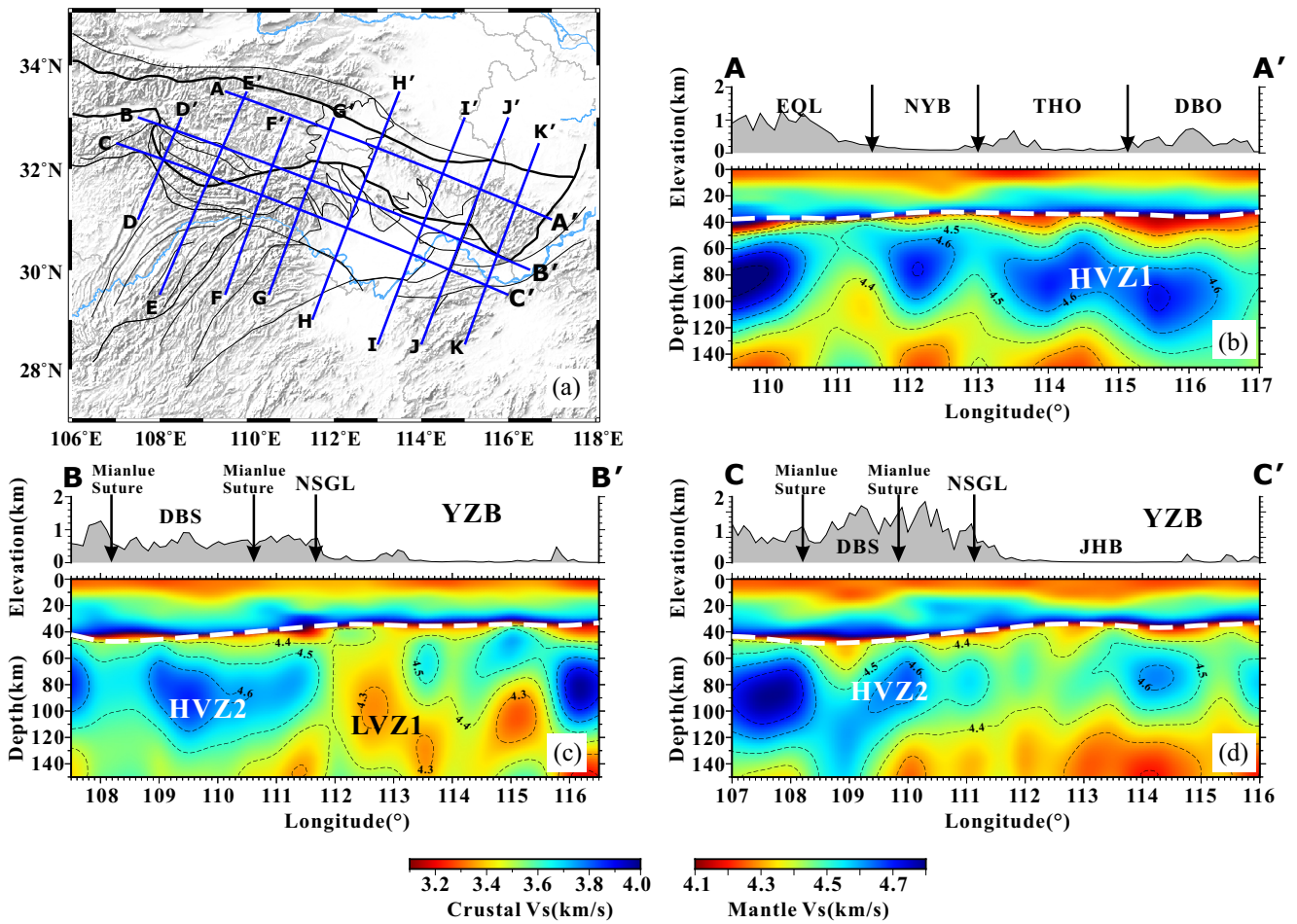

Figure 13. Profiles along the eastern QDOB. The white dotted lines represent the Moho depth. Note that different colour bars are for V_s in the crust and uppermost mantle. The HVZ1, HVZ2 and LVZ1 are consistent with Fig. 11.

5.3 Tectonic implications of DBS

The DBS developed as a typical thrust nappe of the southern Qinling orogen, which displays an arc shape protruding to the southwest in the map view and has a general northwestern trend (Hu *et al.* 2012; Li *et al.* 2015a). At present, it is generally believed that the formation of the DBS and its foreland basin is related to the collision of the Qinling microplate and YZB in the Late Triassic, but its tectonic evolution lasted until the Cenozoic (Dong *et al.* 2008; Hu *et al.* 2012; Shi *et al.* 2012)

Two deep-rooted HVZs beneath the HNMC and SNHL domes were reported based on ambient noise tomography and receiver function analysis (Jiang *et al.* 2016; Guo & Chen 2017; Song *et al.* 2018; Luo *et al.* 2020) and interpreted as a pair of mechanically rigid bodies that compressed and blocked the soft sediments in the upper crust of the Qinling orogen during the formation of the DBS. These two HVZs are also clearly displayed in our new velocity model (Figs 11a–c, 12a and b, 13c and d, 14c and d). The LVZ between the HNMC and SNHL domes gradually enlarges from the upper crust (Figs 11a and 12a) to the middle crust (Figs 11b and 12b) and extends from the SCB to the DBS with a gentle dip from south to north, which may indicate the subduction from the SCB to the DBS (Si *et al.* 2016; Song *et al.* 2018).

A prominent feature in the lower crust beneath the DBS is a high-velocity anomaly (~3.9–4.1 km s^{-1}; Figs 12c and 13c) with thick crust (~55 km) and high V_p/V_s ratio (~1.85, S. Luo *et al.* 2020), which differs from EQL. This feature may indicate mafic lower crust beneath the DBS. Because of the N–S extrusion, the amount of crustal shortening across the DBS is >130 km, which is sufficient to allow the lower crust beneath the DBS to experience eclogite phase transition and increase the density (Li *et al.* 2015a). This may also be the reason for the sustained convergence between the YZB and NCB.

Structural analysis and deep seismic reflection profile studies indicate that the southern DBS is a thin-skinned structure (Dong *et al.* 2008; Hu *et al.* 2012; Li *et al.* 2015a) and several subhorizontal detachment layers have been found in the crust beneath the DBS (Shi *et al.* 2012; Li *et al.* 2013). In the upper mantle, the high-velocity lithospheric mantle extends from the northeastern margin of the SCB to the DBS and reaches Ankang Fault (Figs 12d–f and 14a–c), which shows the thin-skinned structural characteristics of the DBS. The HVZ in the upper mantle has a subhorizontal distribution (Figs 14a and b). The decreasing metamorphic temperatures and pressures from the DBO through the THO to the EQL indicate deep subduction in the east and shallow subduction in the west (Liu *et al.* 2010; Wu & Zheng 2013). Therefore, we suggest that the subhorizontal HVZ is due to shallow subduction of the YZB in the DBS region and provides support for the high-velocity lower crust.

Based on the combination of evidence from previous studies and our new velocity model, we suggest that DBS is a thrust nappe structure with high-velocity lower crust, which first formed in the

Downloaded from https://academic.oup.com/gji/article/228/2/1294/6378898 by guest on 24 April 2024

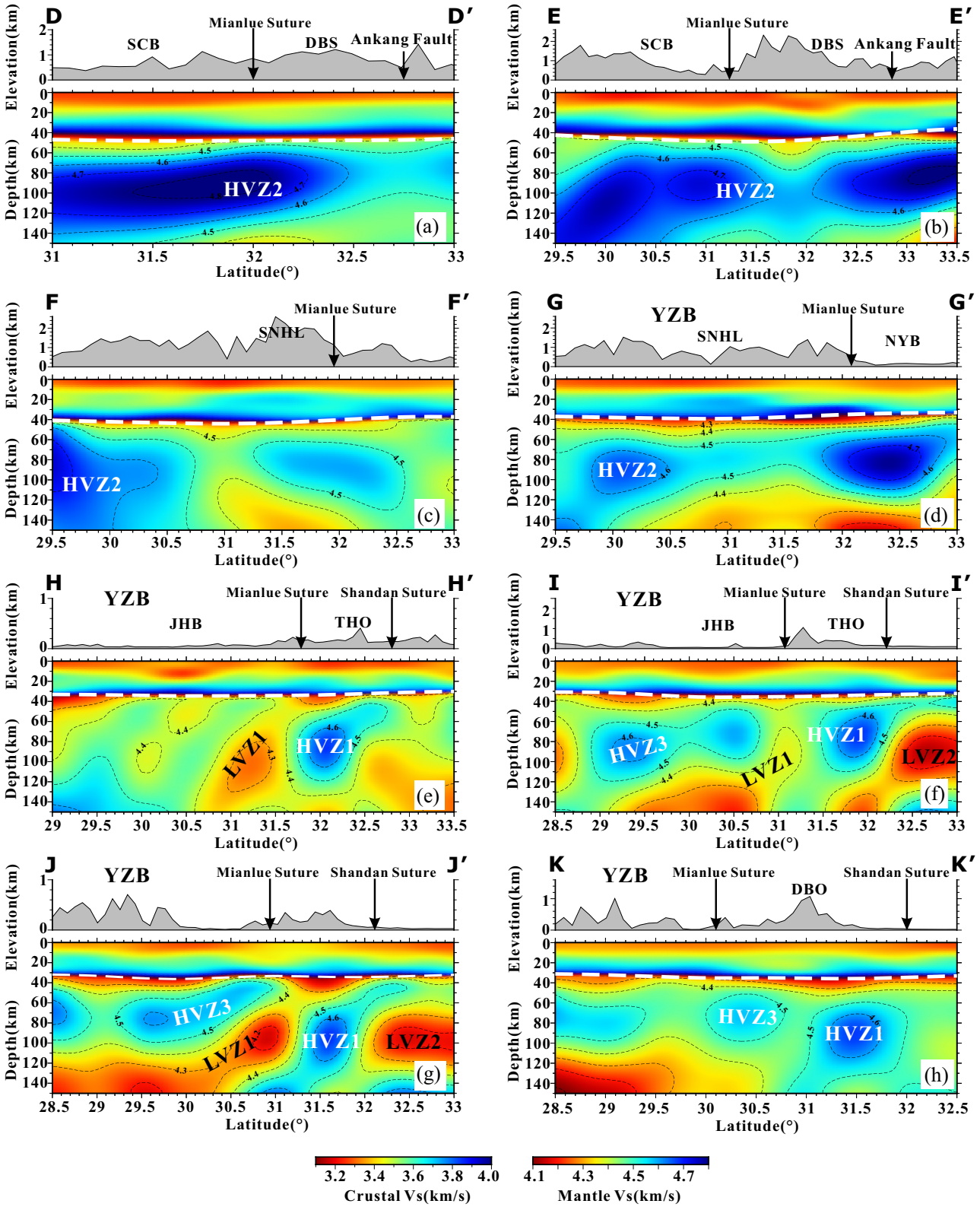

Figure 14. Profiles perpendicular to the east QDOB. The white dotted lines represent the Moho depth. Note that different colour bars are for V_s in the crust and uppermost mantle. The HVZ1, HVZ2, LVZ1 and LVZ2 are consistent with Fig. 11. HVZ3 represent the remnant lithospheric mantle after the destruction beneath YZB.

Downloaded from https://academic.oup.com/gji/article/228/2/1294/6378898 by guest on 24 April 2024

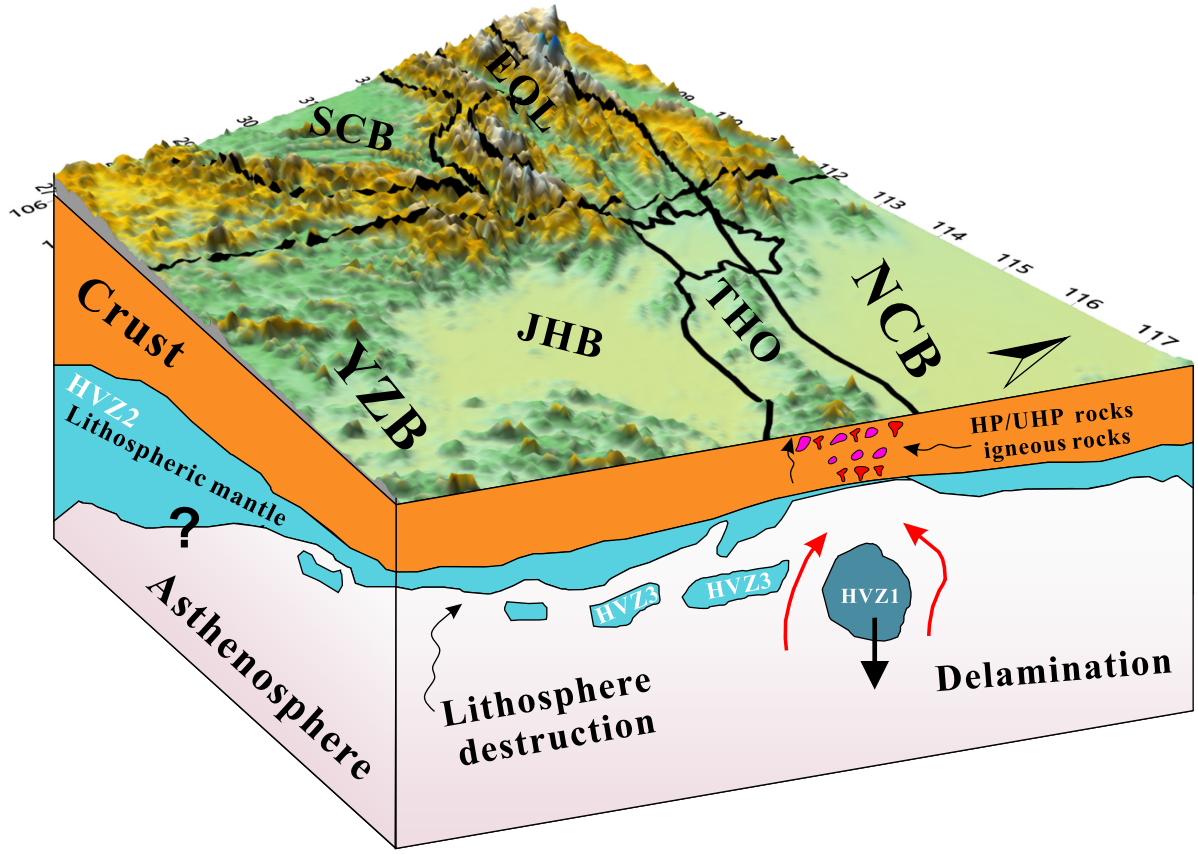

Figure 15. Schematic model for the lower crust delamination and exhumation of UP/HUP metamorphic rocks. HVZ1, HVZ2 and HVZ3 are consistent with Fig. 11.

Late Mesozoic. The HNMC and SNHL acted as a pair of rigid blocks, which compressed and blocked the soft sediments in the upper crust of the Qinling orogen during the formation of the DBS. The crust vertically accreted during the continued convergence between the YZB and the NCB may have caused eclogitization phase transactions in the lower crust that display significant high-velocity anomalies. In the upper mantle, the high-velocity lithospheric mantle extends from the northeastern margin of the SCB to the DBS and reaches the Ankang Fault with a subhorizontal distribution. That means that the compression deformation only occurs in the crust in the DBS, which has thin-skinned structural characteristics due to the shallow subduction of the YZB. In contrast, in lithospheric mantle, the collision is similar to flat subduction and provides support for the high-velocity lower crust.

6 CONCLUSIONS

In this study, we constructed a new S-wave velocity model of the crustal and uppermost mantle beneath the eastern QDOB and its adjacent areas by using ambient noise tomography and seismic data from permanent and portable stations. Our *S*-wave velocity model reveals low velocities in the upper mantle beneath the YZB and NCB (LVZ1 and LVZ2), reflecting the lithospheric destruction. In the orogenic belt, we observed a low velocity anomaly in middle-lower crust beneath EQL, THO and DBO, whereas a high velocity anomaly was observed in the lower crust beneath the DBS. In the upper mantle, a remarkable strip-shaped HVZ (HVZ1) was observed beneath the orogenic belt. The main findings of this study can be summarized as follows:

(1) Similar to the NCB, the lithospheric mantle of the YZB was destroyed. Based on our *S*-wave velocity model, the destruction area of the YZB is bounded by the NSGL.

(2) The low velocity in the middle to lower crust and strip-shaped HVZ in the upper mantle beneath the EQL, THO and DBO reveal that lower crust delamination did not only occur in EQL but also in the THO and DBO. Our results support a two-stage exhumation model for HP/UHP rocks. The breaking away of the slab from the subducted YZB during the Early–Middle Triassic caused the first stage of the HP/UHP rocks exhumation process, and the subsequent lower crust delamination triggered the second stage.

(3) The HNMC and SNHL acted as a pair of rigid blocks and play important roles in the formation of the arc-shaped structure of the DBS. The continued convergence between the YZB and NCB may have caused the eclogitized lower crust, which differs from EQL. The lithospheric mantle extends from the northeastern margin of the SCB to the DBS and has a subhorizontal distribution. It provides support for the high-velocity lower crust of the DBS, which may be due to the shallow subduction of the YZB with thin-skinned structural characteristics.

ACKNOWLEDGMENTS

We thank Xuewei Bao for providing their *S*-wave velocity model. We thank editor Carl Tape and two anonymous reviewers for their

Downloaded from https://academic.oup.com/gji/article/228/2/1294/6378898 by guest on 24 April 2024

constructive reviews that have significantly improved the paper. This study was supported by the National Natural Science Foundation of China (Nos. 41874169, 42074176, U1939204), the Open Research Fund Program of the Key Laboratory of Geospace Environment and Geodesy, Ministry of Education (No. 19–02-05) and the Fundamental Research Funds for the Central Universities (No. 2042020kf0010). Most of the figures are created with the Generic Mapping Tools (GMT; Wessel *et al.* 2013).

DATA AVAILABILITY

The seismic data underlying this paper are available in Data Management Centre of China National Seismic Network at Institute of Geophysics, at https://dx.doi.org/10.11998/SeisDmc/SN.

REFERENCES

Aki, K., 1957. Space and time spectra of stationary stochastic waves, with special reference to microtremors, *Bull. Earthq. Res. Inst.,* **35,** 415–456.

Bao, X. *et al.*, 2013. Crust and upper mantle structure of the North China Craton and the NE Tibetan Plateau and its tectonic implications, *Earth planet. Sci. Lett.,* **369-370,** 129–137.

Bao, X., Song, X. & Li, J., 2015a. High-resolution lithospheric structure beneath Mainland China from ambient noise and earthquake surface-wave tomography, *Earth planet. Sci. Lett.,* **417,** 132–141.

Bao, Z., Wang, C.Y., Zeng, L., Sun, W. & Yao, J., 2015b. Slab break-off model for the Triassic syn-collisional granites in the Qinling orogenic belt, Central China: zircon U-Pb age and Hf isotope constraints, *Int. Geol. Rev.,* **57,** 492–507.

Bensen, G.D. *et al.*, 2007. Processing seismic ambient noise data to obtain reliable broad-band surface wave dispersion measurements, *Geophys. J. Int.,* **169,** 1239–1260.

Borah, K., Rai, S.S., Prakasam, K.S., Gupta, S., Priestley, K. & Gaur, V.K., 2014. Seismic imaging of crust beneath the Dharwar Craton, India, from ambient noise and teleseismic receiver function modelling, *Geophys. J. Int.,* **197,** 748–767.

Brandmayr, E., Kuponiyi, A.P., Arroucau, P. & Vlahovic, G., 2016. Group velocity tomography of the upper crust in the eastern Tennessee seismic zone from ambient noise data, *Tectonophysics,* **688,** 148–156.

Chen, H. & Huang, J., 2017. Numerical simulation on the detachement of eclogitic lower crust, *Sci. Sin. Terrae,* **47,** 82–94.

Chen, H.P., Zhu, L.B., Wang, Q.D., Zhang, P. & Yang, Y.H., 2014. S-wave velocity structure of the North China from inversion of Rayleigh wave phase velocity, *J. Asian Earth Sci.,* **88,** 178–191.

Clements, T. & Denolle, M.A., 2018. Tracking groundwater levels using the ambient seismic field, *Geophys. Res. Lett.,* **45,** 6459–6465.

Deng, Y.F., Chen, L., Xu, T., Wu, J., Romanelli, F. & Panza, G.F., 2017. Lateral variation in seismic velocities and rheology beneath the Qinling-Dabie orogen, *Sci. China Earth Sci.,* **60,** 576–588.

Ditmar, P.G. & Yanovskaya, T.B., 1987. A generalization of the Backus–Gilbert method for estimation of lateral variations of surface wave velocity, *Izv Phys Solid Earth,* **23,** 470–477.

Dong, Y.P., Zha, X.F., Fu, M.Q., Zhang, Q., Yang, Z. & Zhang, Y., 2008. Characteristics of the Dabashan fold-thrust nappe structure at the southern margin of the Qinling, China, *Geol. Bull. China,* **27,** 1493–1508.

Dong, Y., Zhang, G., Neubauer, F., Liu, X., Genser, J. & Hauzenberger, C., 2011. Tectonic evolution of the Qinling orogen, China: review and synthesis, *J. Asian Earth Sci.,* **41,** 213–237.

Dong, Y. *et al.*, 2015. Propagation tectonics and multiple accretionary processes of the Qinling Orogen, *J. Asian Earth Sci.,* **104,** 84–98.

Ekström, G., Abers, G.A. & Webb, S.C., 2009. Determination of surface-wave phase velocities across USArray from noise and Aki's spectral formulation, *Geophys. Res. Lett.,* **36,** doi:10.1029/2009GL039131.

Enkelmann, E. *et al.*, 2006. Cenozoic exhumation and deformation of northeastern Tibet and the Qinling: is Tibetan lower crustal flow diverging around the Sichuan basin? *Bull. geol. Soc. Am.,* **118,** 651–671.

Ernst, W.G., Tsujimori, T., Zhang, R. & Liou, J.G., 2007. Permo-Triassic collision, subduction-zone metamorphism, and tectonic exhumation along the East Asian continental margin, *Annu. Rev. Earth planet. Sci.,* **35,** 73–110.

Gao, S., Zhang, B., Jin, Z. & Kern, H., 1999. Lower crustal delamination in the Qinling-Dabie orogenic belt, *Sci. China, Ser., D Earth Sci.,* **42,** 423–433.

Gao, S., Xu, W., Zhang, J. & Liu, Y., 2009. Delamination and destruction of the North China Craton, *Chinese Sci. Bull.,* **54,** 1962–1973.

Guo, Z. & Chen, Y.J., 2016. Crustal structure of the eastern Qinling orogenic belt and implication for reactivation since the Cretaceous, *Tectonophysics,* **683,** 1–11.

Guo, Z. & Chen, Y.J., 2017. Mountain building at northeastern boundary of Tibetan Plateau and craton reworking at Ordos block from joint inversion of ambient noise tomography and receiver functions, *Earth planet. Sci. Lett.,* **463,** 232–242.

Guo, Z., Gao, X., Shi, H. & Wang, W., 2013. Crustal and uppermost mantle S-wave velocity structure beneath the japanese islands from seismic ambient noise tomography, *Geophys. J. Int.,* **193,** 394–406.

Hacker, B.R. *et al.*, 2000. Exhumation of ultrahigh-pressure continental crust in east central China: late Triassic-Early Jurassic tectonic unroofing, *J. geophys. Res.,* **105,** 13 339–13 364.

He, C. & Zheng, Y.F., 2018. Seismic evidence for the absence of deeply subducted continental slabs in the lower lithosphere beneath the Central Orogenic Belt of China, *Tectonophysics,* **723,** 178–189.

He, C., Dong, S., Chen, X., Santosh, M. & Li, Q., 2014a. Crustal structure and continental dynamics of Central China: a receiver function study and implications for ultrahigh-pressure metamorphism, *Tectonophysics,* **610,** 172–181.

He, R., Shang, X., Yu, C., Zhang, H. & Hilst, R.D.Van der, 2014b. A unified map of Moho depth and Vp/Vs ratio of continental china by receiver function analysis, *Geophys. J. Int.,* **199,** 1910–1918.

Herrmann, R.B., 2013. Computer programs in seismology: an evolving tool for instruction and research, *Seismol. Res. Lett.,* **84,** 1081–1088.

Herrmann, R.B. & Ammon, C., 2004. Surface Waves, Receiver Functions and Crustal Structure, Computer Programs in Seismology, Version 3.30. Saint Louis University, Saint Louis. Available at: http://www.eas.slu.edu/People/RBHerrmann/CPS330.html.

Hu, F., Liu, S., Ducea, M.N., Chapman, J.B., Wu, F. & Kusky, T., 2020. Early Mesozoic magmatism and tectonic evolution of the Qinling Orogen: implications for oblique continental collision, *Gondwana Res.,* **88,** 296–332.

Hu, J., Chen, H., Qu, H., Wu, G., Yang, J. & Zhang, Z., 2012. Mesozoic deformations of the Dabashan in the southern Qinling orogen, central China, *J. Asian Earth Sci.,* **47,** 171–184.

Huang, R., Zhu, L. & Xu, Y., 2014. Crustal structure of Hubei Province of China from teleseismic receiver functions: evidence for lower crust delamination, *Tectonophysics,* **636,** 286–292.

Jiang, C., Yang, Y. & Zheng, Y., 2016. Crustal structure in the junction of Qinling Orogen, Yangtze Craton and Tibetan Plateau: implications for the formation of the Dabashan Orocline and the growth of Tibetan Plateau, *Geophys. J. Int.,* **205,** 1670–1681.

Jiang, G., Zhang, G., Zhao, D., Lü, Q., Li, H. & Li, X., 2015. Mantle dynamics and Cretaceous magmatism in east-central China: insight from teleseismic tomograms, *Tectonophysics,* **664,** 256–268.

Jiang, M., Ai, Y., Chen, L. & Yang, Y., 2013. Local modification of the lithosphere beneath the central and western North China Craton: 3-D constraints from Rayleigh wave tomography, *Gondwana Res.*, **24,** 849–864.

Kern, H., Gao, S., Jin, Z., Popp, T. & Jin, S., 1999. Petrophysical studies on rocks from the Dabie ultrahigh-pressure (UHP) metamorphic belt, Central China: implications for the composition and delamination of the lower crust, *Tectonophysics,* **301,** 191–215.

Lebedev, S. & Nolet, G., 2003. Upper mantle beneath Southeast Asia from S velocity tomography, *J. geophys. Res.,* **108,** doi:10.1029/2000jb000073.

Lecocq, T., Caudron, C. & Brenguier, F., 2014. Msnoise, a python package for monitoring seismic velocity changes using ambient seismic noise, *Seismol. Res. Lett.,* **85,** 715–726.

Downloaded from https://academic.oup.com/gji/article/228/2/1294/6378898 by guest on 24 April 2024

Li, J., Zhang, Y., Dong, S. & Shi, W., 2013. Structural and geochronological constraints on the Mesozoic tectonic evolution of the North Dabashan zone, South Qinling, central China, *J. Asian Earth Sci.,* **64,** 99–114.

Li, J., Dong, S., Yin, A., Zhang, Y. & Shi, W., 2015a. Mesozoic tectonic evolution of the Daba Shan Thrust Belt in the southern Qinling orogen, central China: constraints from surface geology and reflection seismology, *Tectonics,* **34,** 1545–1575.

Li, S., Li, Q., Hou, Z., Yang, W. & Wang, Y., 2005. Cooling history and exhumation mechanism of the ultrahigh-pressure metamorphic rocks in the Dabie mountains, central China, *Acta Petrol. Sin.,* **21,** 1117–1124.

Li, S. *et al.*, 2015b. Coupling and transition of Meso-Cenozoic intracontinental deformation between the Taihang and Qinling Mountains, *J. Asian Earth Sci.,* **114,** 188–202.

Li, S. *et al.*, 2017a. Triassic southeastward subduction of North China Block to South China Block: insights from new geological, geophysical and geochemical data, *Earth-Sci. Rev.,* **166,**270–285.

Li, X., Zhu, P., Kusky, T.M., Gu, Y., Peng, S., Yuan, Y. & Fu, J., 2015c. Has the Yangtze craton lost its root? A comparison between the North China and Yangtze cratons, *Tectonophysics,* **655,** 1–14.

Li, Y., Wu, Q., Zhang, R., Pan, J., Zhang, F. & Zeng, R., 2009. The lithospheric thinning of the North China Craton inferred from Rayleigh waves inversion, *Geophys. J. Int.,* **177,** 1334–1342.

Li, Y., Pan, J., Wu, Q. & Ding, Z., 2017. Lithospheric structure beneath the northeastern Tibetan Plateau and the western Sino-Korea Craton revealed by Rayleigh wave tomography, *Geophys. J. Int.,* **210,** 570–584.

Lin, F.C., Moschetti, M.P. & Ritzwoller, M.H., 2008. Surface wave tomography of the western United States from ambient seismic noise: rayleigh and Love wave phase velocity maps, *Geophys. J. Int.,* **173,** 281–298.

Liu, S., Steel, R. & Zhang, G., 2005. Mesozoic sedimentary basin development and tectonic implication, northern Yangtze Block, eastern China: record of continent-continent collision, *J. Asian Earth Sci.,* **25,** 9–27.

Liu, X., Jahn, B. ming, Dong, S., Lou, Y. & Cui, J., 2008. High-pressure metamorphic rocks from Tongbaishan, central China: u-Pb and 40Ar/39Ar age constraints on the provenance of protoliths and timing of metamorphism, *Lithos,* **105,** 301–318.

Liu, X., Jahn, B. ming, Cui, J., Li, S., Wu, Y. & Li, X. hua., 2010. Triassic retrograded eclogites and Cretaceous gneissic granites in the Tongbai Complex, central China: implications for the architecture of the HP/UHP Tongbai-Dabie-Sulu collision zone, *Lithos,* **119,** 211–237.

Liu, X., Li, S. & Jahn, B. ming., 2015. Tectonic evolution of the Tongbai-Hong'an orogen in central China: from oceanic subduction/accretion to continent-continent collision, *Sci. China Earth Sci.,* **58,** 1477–1496.

Luo, S., Huang, R., Zhu, L. & Yao, H., 2020. The formation of the Dabashan orocline, central China: insights from high-resolution 3D crustal shear-wave velocity structure, *Tectonophysics,* **774,** 228244.

Luo, Y., Xu, Y. & Yang, Y., 2012. Crustal structure beneath the Dabie orogenic belt from ambient noise tomography, *Earth planet. Sci. Lett.,* **313-314,** 12–22.

Luo, Y., Xu, Y. & Yang, Y., 2013. Crustal radial anisotropy beneath the dabie orogenic belt from ambient noise tomography, *Geophys. J. Int.,* **195,** 1149–1164.

Luo, Y., Zhao, K., Tang, C.C. & Xu, Y., 2018. Seismic evidence for multiple-stage exhumation of high/ultrahigh pressure metamorphic rocks in the eastern Dabie orogenic belt, *Geophys. J. Int.,* **214,** 1379–1390.

Ma, C., Li, Z., Ehlers, C., Yang, K. & Wang, R., 1998. A post-collisional magmatic plumbing system: mesozoic granitoid plutons from the Dabieshan high-pressure and ultrahigh-pressure metamorphic zone, east-central China, *Lithos,* **45,** 431–456.

Mattauer, M. *et al.*, 1985. Tectonics of the Qinling Belt: build-up and evolution of eastern Asia, *Nature,* **317,** 496–500.

Meng, Q.R., 2017. Origin of the Qinling Mountains, *Sci. Sin. Terrae,* **47,** 412–420.

Meng, Q.R. & Zhang, G.W., 2000. Geologic framework and tectonic evolution of the Qinling orogen, central China, *Tectonophysics,* **323,** 183–196.

Niu, P.P. & Jiang, S.Y., 2020. Petrogenesis of the Late Mesozoic Qijinfeng Granite Complex in the Tongbai orogen: geochronological, geochemical and Sr-Nd-Pb-Hf isotope evidence, *Lithos,* **356–357,** doi:10.1016/j.lithos.2019.105290.

Oh, C.W. & Lee, B.C., 2019. The relationship between systematic metamorphic patterns and collisional processes along the qinling-sulu-odesan collisional belt between the North and South China Cratons, in *Geol. Soc. Spec. Publ.,* Vol., **478,** pp. 449–475.

Pasyanos, M.E., Masters, T.G., Laske, G. & Ma, Z., 2014. LITHO1.0: an updated crust and lithospheric model of the Earth, *J. geophys. Res.,* **119,** 2153–2173.

Prieto, G.A., Lawrence, J.F. & Beroza, G.C., 2009. Anelastic Earth structure from the coherency of the ambient seismic field, *J. geophys. Res.,* **114,** doi:10.1029/2008JB006067.

Sadeghisorkhani, H., Gudmundsson, Ó. & Tryggvason, A., 2018. GSpecDisp: a matlab GUI package for phase-velocity dispersion measurements from ambient-noise correlations, *Comput. Geosci.,* **110,** 41–53.

Saygin, E. & Kennett, B.L.N., 2010. Ambient seismic noise tomography of Australian continent, *Tectonophysics,* **481,** 116–125.

Shapiro, N.M. & Campillo, M., 2004. Emergence of broadband Rayleigh waves from correlations of the ambient seismic noise, *Geophys. Res. Lett.,* **31,** doi:10.1029/2004GL019491.

Shen, X., Kind, R., Huang, Z., Yuan, X. & Liu, M., 2019. Imaging the Mantle Lithosphere below the China cratons using S-to-p converted waves, *Tectonophysics,* **754,** 73–79.

Shi, W., Zhang, Y., Dong, S., Hu, J., Wiesinger, M., Ratschbacher, L., Jonckheere, R. *et al.*, 2012. Intra-continental Dabashan orocline, southwestern Qinling, Central China, *J. Asian Earth Sci.,* **46,** 20–38.

Si, X., Teng, J.W., Liu, Y.S., Ma, X.Y., Qiao, Y.H., Dong, X.P. & Song, P.H., 2016. Crust structure of the Qinling orogenic and the region on its north and south margins from teleseismic receiver function, *Acta Geophys. Sin.,* **59,** 1321–1334.

Song, P. *et al.*, 2018. Flyover Crustal Structures Beneath the Qinling Orogenic Belt and Its Tectonic Implications, *J. geophys. Res.,* **123,** 6703–6718.

Teng, J.W. *et al.*, 2014. Fine velocity structures and deep processes in crust and mantle of the Qinling orogenic belt and the adjacent North China craton and Yangtze craton, *Acta Geophys. Sin.,* **57,** 3154–3175.

Tsai, V.C. & Moschetti, M.P., 2010. An explicit relationship between time-domain noise correlation and spatial autocorrelation (SPAC) results, *Geophys. J. Int.,* **182,** 454–460.

Wang, H.L., Bai, W.M. & Wang, Q.P., 2011. Numerical simulation of lithosphere delamination at the continental orogenic belts, *Acta Geophys. Sin.,* **54,** 2851–2863.

Wang, Q., Ji, S., Salisbury, M.H., Xia, B., Pan, M. & Xu, Z., 2005. Pressure dependence and anisotropy of P-wave velocities in ultrahigh-pressure metamorphic rocks from the Dabie-Sulu orogenic belt (China): implications for seismic properties of subducted slabs and origin of mantle reflections, *Tectonophysics,* **398,** 67–99.

Wang, Q.S., Teng, J.W., Zhang, Y.Q., Wen, W. & Hua, C.C., 2013a. Discussion on the special gravity field across the north part of Middle Qinling Mt, *Acta Geophys. Sin.,* **56,** 792–798.

Wang, Q.S., Teng, J.W., Zhang, Y.Q., Yang, H., Zhao, B. Bin & Hu, G.Z., 2013b. Discussion on gravity anomalies and crustal structure of the middle Qinling Mountains, *Acta Geophys. Sin.,* **56,** 3999–4008.

Wang, Q.Y., Brenguier, F., Campillo, M., Lecointre, A., Takeda, T. & Aoki, Y., 2017. Seasonal Crustal Seismic Velocity Changes Throughout Japan, *J. Geophys. Res. Solid Earth,* **122,** 7987–8002.

Wessel, P., Smith, W.H.F., Scharroo, R., Luis, J. & Wobbe, F., 2013. Generic mapping tools: improved version released, *Eos (Washington. DC).,* **94,** 409–410.

Wu, T., Zhang, S., Li, M., Qin, W. & Zhang, C., 2016. Two crustal flowing channels and volcanic magma migration underneath the SE margin of the Tibetan Plateau as revealed by surface wave tomography, *J. Asian Earth Sci.,* **132,** 25–39.

Wu, T., Zhang, S., Cao, Z., Li, M., Hua, Y., Fu, X. & Wei, Y., 2020. Lithospheric structure of Hubei Province, central China, from Rayleigh wave tomography: insight into the spatial contact relationship between the Yangtze Plate and the eastern Qinling-Dabie orogenic belt, *Geophys. J. Int.,* **221,** 1669–1683.

Wu, Y., 2009. Multistage evolution of continental collision orogen: a case study for western Dabie orogen, *Chinese Sci. Bull.,* **54,** 2568–2579.

Downloaded from https://academic.oup.com/gji/article/228/2/1294/6378898 by guest on 24 April 2024

Wu, Y. & Zheng, Y., 2013. Tectonic evolution of a composite collision orogen: an overview on the Qinling-Tongbai-Hong'an-Dabie-Sulu orogenic belt in central China, *Gondwana Res.*, **23,** 1402–1428.

Xin, H., Zhang, H., Gao, L., Gao, J., Kang, M. & He, R., 2019. High-resolution lithospheric velocity structure of continental China by double-difference seismic travel-time tomography, *Seismol. Res. Lett.,* **90,** 229–241.

Xu, W.L., Zhou, Q.J., Pei, F.P., Yang, D. Bin, Gao, S., Li, Q.L. & Yang, Y.H., 2013. Destruction of the North China Craton: delamination or thermal/chemical erosion? Mineral chemistry and oxygen isotope insights from websterite xenoliths, *Gondwana Res.*, **23,** 119–129.

Yang, F., Santosh, M. & Kim, S.W., 2018. Mesozoic magmatism in the eastern North China Craton: insights on tectonic cycles associated with progressive craton destruction, *Gondwana Res.*, **60,** 153–178.

Yanovskaya, T.B., 1997. Resolution estimation in the problems of seismic ray tomography, *Izv. - Phys. Solid Earth,* **33,** 762–765.

Yanovskaya, T.B. & Ditmar, P.G., 1990. Smoothness criteria in surface wave tomography, *Geophys. J. Int.,* **102,** 63–72.

Yao, H., Hilst, R.D. van der & Hoop, M.V.de., 2006. Surface-wave array tomography in SE Tibet from ambient seismic noise and two-station analysis - I. Phase velocity maps, *Geophys. J. Int.,* **166,** 732–744.

Yuan, X.C., Klemperer, S.L., Teng, W.B., Liu, L.X. & Chetwin, E., 2003. Crustal structure and exhumation of the Dabie Shan ultrahigh-pressure orogen, eastern China, from seismic reflection profiling, *Geology,* **31,** 435–438.

Zertani, S., John, T., Tilmann, F., Motra, H.B., Keppler, R., Andersen, T.B. & Labrousse, L., 2019. Modification of the seismic properties of subducting continental crust by eclogitization and deformation processes, *J. geophys. Res.,* **124,** 9731–9754.

Zhang, G., Zhang, Z. & Dong, Y., 1995. Nature of the main tectonolithostratigraphic units of the Qinling orogen: implications for tectonic evolution, *Acta Petrol. Sin.,* **11,** 101–114.

Zhang, G., Guo, A., Liu, F., Xiao, Q. & Meng, Q., 1996a. The 3D structures of Qinling Orogenic Belts and its geodynamic implications, *Sci. China, Ser. D,* **26,** 3–8.

Zhang, G., Meng, Q., Yu, Z., Sun, Y., Zhou, D. & Guo, A., 1996b. Orogenesis and dynamics of the Qinling orogen, *Sci. China, Ser., D Earth Sci.,* **39,** 196–200.

Zhang, J., Ma, C., Li, J., She, Z. & Zhang, C., 2013. Geochronology and geochemistry of the Early Cretaceous Jigongshan and Qijianfeng batholiths in the Tongbai orogen, central China: implications for lower crustal delamination, *Int. J. Earth Sci.,* **102,** 1045–1067.

Zhang, X., Teng, J., Sun, R., Romanelli, F., Zhang, Z. & Panza, G.F., 2014. Structural model of the lithosphere-asthenosphere system beneath the Qinghai-Tibet Plateau and its adjacent areas, *Tectonophysics,* **634,** 208–226.

Zhang, Z. *et al.*, 2009. Crustal structure across the Three Gorges area of the Yangtze platform, central China, from seismic refraction/wide-angle reflection data, *Tectonophysics,* **475,** 423–437.

Zhao, K., Luo, Y., Yang, Y. & Yang, X., 2021. High-resolution lithospheric structures of the Qinling-Dabie orogenic belt: implications for deep subduction and delamination of continental lithosphere, *Tectonophysics,* **806,** 228799, Elsevier B.V.

Zhao, Z. *et al.*, 2011. Delamination and ultra-deep subduction of continental crust: constraints from elastic wave velocity and density measurement in ultrahigh-pressure metamorphic rocks, *J. Metamorph. Geol.,* **29,** 781–801.

Downloaded from https://academic.oup.com/gji/article/228/2/1294/6378898 by guest on 24 April 2024